1D Pd-Based Nanomaterials as Efficient Electrocatalysts for Fuel Cells

Yizhong Lu and Wei Chen

Abstract Since the first experiment conducted by William Grove in 1839, fuel cell, a device that converts the chemical energy stored in fuels into electricity through electrochemical reactions with oxygen or other oxidizing agents, has attracted worldwide attention in the past few decades. However, despite extensive research progress, the widespread commercialization of fuel cells is still a big challenge partly because of the low catalytic performance and high-cost of the Pt-based electrocatalysts. In addition, the hydrogen storage is another critical issue for the commercialization of hydrogen-powered fuel cells. Among the metal catalysts, Pd has been found to be a promising alternative because of its excellent catalytic properties and lower cost than Pt. Moreover, Pd-based materials exhibit high hydrogen storage capabilities. In this chapter, we summarize recent progress in the synthesis of one-dimensional (1D) Pd-based nanomaterials and their applications as electrocatalysts on both anodic and cathodic sides of fuel cells, and their applications in hydrogen storage. We demonstrated here that various 1D Pd-based nanomaterials, such as nanorods, nanowires, and nanotubes have been successfully prepared through different synthetic routes. The nanostructured 1D Pd-based materials exhibit high catalytic performance for electrooxidation of small organic molecules and oxygen reduction reaction (ORR). Moreover, high capacities for hydrogen storage have also been reported with 1D Pd-based nanomaterials.

Y. Lu · W. Chen (✉)
State Key Laboratory of Electroanalytical Chemistry, Changchun Institute of Applied Chemistry, Chinese Academy of Sciences, Changchun 130022, Jilin, China
e-mail: weichen@ciac.ac.cn

Y. Lu
University of Chinese Academy of Sciences, Beijing 100039, China

1 Introduction

Due to the increasing worldwide energy demand and environmental concerns, much effort has been devoted to the seeking for efficient and clean energy sources to replace the traditional fossil fuels such as gasoline and diesel [1]. Fuel cell, a device that converts the chemical energy stored in fuels into electricity through electrochemical reactions efficiently without pollution, has been attracting increasing research interest as a new power source for portable applications due to their high energy-conversion efficiency and relatively low operating temperature [2, 3]. Based on the operating temperature and the type of used electrolyte, fuel cells are usually classified into phosphoric-acid fuel cells (PAFCs), solid oxide fuel cells (SOFCs), alkaline fuel cells (AFCs), molten-carbonate fuel cells (MCFCs), polymer exchange membrane fuel cells (PEMFCs), and direct-methanol fuel cells (DMFCs) [4]. While all types of fuel cells work on the similar principle: hydrogen or other fuels oxidation at anode and oxygen reduction at cathode. Among different types of fuel cells, the PEMFCs and DMFCs are especially promising for automotive and portable electronic applications owing to the low operation temperatures [5, 6]. It should be noted that despite extensive research progress, there are still many scientific and technological challenges to realize the widespread commercialization of fuel cells. For instance, the reactions on both anode and cathode need electrocatalysts with high catalytic performance. To improve the efficiency and durability, and to reduce the cost of fuel cells, the conventional Pt catalysts have to be replaced by novel nanostructured electrocatalysts with high electrocatalytic activity, high stability, and low-cost. For fuel cells, platinum has been regarded as the best electrocatalyst because of the highest electrocatalytic activity among the metal catalysts for electrooxidation of small organic fuels and for oxygen reduction [7]. However, with platinum as an anode catalyst, its surface is usually heavily poisoned by CO intermediates produced during the oxidation of organic fuels, resulting in the lowering of catalytic performance. On the other hand, the state-of-the-art cathode electrocatalysts, Pt nanoparticles (2–5 nm) supported on amorphous carbon materials (Pt/C), usually suffer from poor durability caused by the fast and significant loss of platinum electrochemical surface area (ECSA) over time during fuel cell operation. Moreover, the high price and the limited global supply of Pt largely drive up the cost of fuel cells. To reduce the cost and minimize the self-poisoning of catalysts, Pt-based electrocatalysts alloyed with other transition metals (Fe, Co, Ni, Cu, Mn, Ir) with controlled surface composition and structures have been extensively studied in recent years [8–17]. Compared to pure platinum, Pt-based electrocatalysts exhibit higher performance and a reduced sensitivity toward CO poisoning because of the so-called bifunctional mechanism [18–20] or ligand effect [21, 22]. For instance, Pt-Ru alloys have shown enhanced electrocatalytic activity for fuel cell anode reactions and the enhancement could be well explained by the ligand effect and the bifunctional mechanism [23, 24]. Based on the ligand effect, the presence of ruthenium was proposed to alter the electronic properties of Pt, resulting in less strongly CO adsorption on the catalyst surface. While according to the bifunctional

mechanism, ruthenium provides oxygen-containing species, which could then oxidize CO on the adjacent platinum sites at more negative potentials than pure platinum. Due to the large surface area, various Pt-based bimetallic nanostructures have been synthesized and applied to both anode and cathode catalysts. For example, Xia and co-workers [25] synthesized Pd–Pt bimetallic nanodendrites, which exhibited enhanced catalytic activity for oxygen electro-reduction. Recently, Stamenkovic et al. [12] demonstrated that extended single crystal surfaces of $Pt_3Ni(111)$ exhibit an enhanced ORR activity that is 10-fold higher than the corresponding Pt(111) surface and 90-fold more active than the current state-of-the-art Pt/C catalysts for PEMFCs. Such a remarkable activity was attributed to the unusual electronic structure (d-band center position) and arrangement of surface atoms in near-surface region. For the anode reaction, Yang et al. [10] have found that the (100) facet-terminated Pt_3Co nanocubes are much more active than the Pt nanocubes due to the weaker and slower CO adsorption.

In recent years, to further reduce the loading of Pt, intensive studies have focused on low-Pt or non-Pt electrocatalysts [26–37]. Among the studied non-platinum electrocatalysts, Pd-based nanomaterials have become hot research topics as electrocatalysts in fuel cells because of their similar intrinsic properties to platinum, such as the valence band structure and lattice parameters [38, 39]. More significantly, compared to Pt, Pd is cheaper and exhibits higher electrochemical stability. Recent research progress in Pd-based catalysts has revealed that Pd can catalyze the oxidation of formic acid and alcohols at the anode of polymer electrolyte membrane fuel cells (PEMFCs) with greater tolerance to CO than Pt catalysts and comparable activity toward the cathode oxygen reduction [40–50].

For catalysts on nanoscale, their catalytic efficiency, selectivity and reaction durability are highly dependent on the size, shape, composition, and surface structure [8, 26, 41, 51–54]. Similarly to Pt-based nanoalloys, Pd-based alloy nanomaterials have also shown enhanced electrocatalytic activities compared to pure Pd catalyst due to the synergistic effect or the modulation effect [55, 56]. Recent investigations have found that alloying Pd with some transition metals, such as Au [57], Ag [58], Fe [59], Co [60], Ti [55, 61], Ni [62], Sn [63], etc., is an effective way to improve the catalytic activity of Pd metal. At the same time, some of Pd alloys exhibited comparable activity and stability to those of Pt catalysts.

Among various Pd or Pd-based nanomaterials, one-dimensional (1D) nano-structured electrocatalysts, such as nanowires (NWs) [64–72], nanorods (NRs) [44, 73], nanoleaves (NLs) [74], and nanotubes (NTs) [75–80], have attracted more and more attention in recent years due to their unique structures and high surface area. From a structural perspective, 1D Pd nanomaterials possess largely pristine surfaces with long segments of crystalline planes, as compared with their corresponding 0D morphologies. Additionally, the anisotropic growth of 1D structured materials typically results in the preferential surface display of low energy crystal facets in order to minimize the surface energy of the systems [81]. In the previous studies on 1D Pd nanostructures, high resolution transmission electron microscopy (HRTEM) and selected-area-electron diffraction patterns (SAED) showed that the surfaces of the Pd nanowires are enclosed by {111} and {200} planes, suggesting

the <110> growth direction of the nanowires [82]. It is well known that the catalytic activities of metal nanomaterials are strongly dependent on their exposed surface facets. Earlier studies have shown that the Pd(100) plane exhibits the highest catalytic activity for formic acid oxygen among the three low-index faces Pd(111), Pd(100), and Pd(110) [83, 84]. On the other hand, the single-crystalline 1D nanomaterials with structural anisotropy contain fewer surface defect sites in comparison with the corresponding zero-dimensional nanoparticles. When used as electrocatalysts, the electron transport properties of catalyst materials are of importance for the electrochemical reactions. Compared to metal nanoparticles, 1D nanomaterials can provide more efficient electron transfer, thus lowering the electronic resistance and enhancing the fuel oxidation or Oxygen reduction reactions [76, 85]. Meanwhile, for nanoparticle-based electrocatalysts, the electrochemical scanning process may lead to the particle aggregation, dissolution, and Oswald ripening, which is one of the biggest challenges in designing efficient fuel cell electrocatalysts. However, for 1D nanomaterials, the asymmetric structure nature can effectively prevent their structure destruction from aggregation, dissolution, and ripening [75, 86, 87]. From above, the large surface area, high electrochemical stability, efficient electron transport, and excellent CO-tolerance of 1D Pd-based nanomaterials would be highly advantageous for their applications in fuel cells as anode and cathode catalysts.

Among the fuels fed to the anode of fuel cells, hydrogen is considered to be one of the most promising clean energy carriers due to its light weight, high energy density, and no harmful chemical by-products from its combustion. Hydrogen can be generated from renewable sources, such as water splitting via photolysis [88–92]. For hydrogen powered fuel cells, despite prodigious efforts, how to develop a safe and easy storage method is still a remaining significant challenge for the widespread application of hydrogen as the fuel of choice in mobile transportation. The efficient and safe storage of hydrogen is crucial for promoting the "hydrogen economy". The safety and cost issues of conventional hydrogen storage as compressed gas or liquid largely limit the practical use of these methods. Other developed methods for hydrogen storage by physical adsorption on materials with large surface area or formation of chemical bonds have been proved to be efficient, convenient, and safe approaches [93]. Among the hydrogen storage materials, Pd-based nanomaterials exhibited excellent storage capacity and their storage properties are strongly related to the morphologies, composition, and size of the nanostructures [94].

In this chapter, we highlight the recent progress of one-dimensional Pd-based nanomaterials, including the synthetic techniques and their application in fuel cells as electrocatalysts on both anode and cathode sides. With different preparation routes, various structured nanomaterials with different surface morphologies can be realized. Since the composition and surface structure of Pd-based alloy materials play decisive roles in determining their electrocatalytic properties, the structure and properties of 1D Pd materials can be manipulated by changing synthetic conditions to meet the scientific and technological demands of fuel cell catalysts. In addition, the application of one-dimensional Pd-based nanomaterials in the hydrogen storage

is also discussed here due to their importance in fuel cells. Finally, a brief conclusion and an outlook will be given on the future research directions of 1D Pd-based nanomaterial as efficient electrocatalysts and hydrogen storage materials.

## 2 One-Dimensional Pd-Based Nanomaterials as Effective Cathode Electrocatalysts

From the previous studies, the ORR is considered to proceed by the efficient four-electron pathway or the less efficient two-step pathway, depending on the electrolyte and the catalytic activity of the cathode materials [95].

A. Direct 4-electron pathway:

In alkaline solutions

$$O_2 + 2H_2O + 4e^- \rightarrow 4OH^- \tag{1}$$

Acid solutions.

$$O_2 + 4H^+ + 4e^- \rightarrow 2H_2O \tag{2}$$
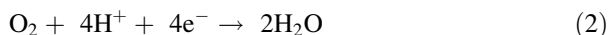
B. Peroxide pathway:

In alkaline solutions

$$O_2 + H_2O + 2e^- \rightarrow HO_2^- + OH^- \tag{3}$$
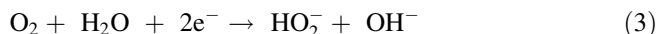
followed by either the further reduction reaction

$$HO_2^- + H_2O + 2e^- \rightarrow 3OH^- \tag{4}$$

or the decomposition reaction

$$2HO_2^- \rightarrow 2OH^- + O_2 \tag{5}$$

In acid solutions

$$O_2 + 2H^+ + 2e^- \rightarrow H_2O_2 \tag{6}$$

followed by either

$$H_2O_2 + 2H^+ + 2e^- \rightarrow 2H_2O \tag{7}$$

or

$$2H_2O_2 \rightarrow 2H_2O + O_2 \tag{8}$$
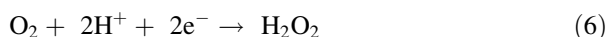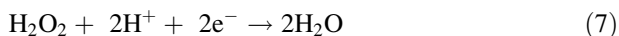
On the basis of the mechanism of ORR, O_2 molecules are firstly adsorbed on the surface of catalysts, and then electrochemically reduced either directly to water or indirectly to intermediate of H_2O_2. According to the previous studies on the Pd and Pt-catalyzed ORR, the adsorption energy (AE) of O adsorption can serve as a good descriptor for the catalytic activity of the catalyst surface toward the ORR [56, 96]. Therefore, it would be of great interest to develop a robust and practical Pd or Pd-based catalysts with low AE toward O species. Recently, Abruna et al. [44] succeeded in tailoring the morphology of the deposited Pd from nanoparticles to nanorods by simply adjusting the precursor concentration in the electrochemical deposition of Pd. They found that the surface-specific activity of Pd nanorods (Pd NRs) toward ORR is not only higher than that of Pd nanoparticles (Pd NPs), but also becomes comparable to that of bulk Pt catalysts under fuel cell operating potentials. It can be seen from Fig. 1a, b that, under the experimental conditions of 1×10^{-5} M $PdCl_2$ precursor and 3000 s electrochemical deposition time, only Pd nanoparticles were formed with the size range from 5 to 10 nm. However, when the $PdCl_2$ concentration increased to 3×10^{-4} M and deposition time decreased to 100 s, uniform Pd nanorods can be produced with an average diameter of 5 nm and an aspect ratio of ~ 8. By comparing the electrocatalytic activities of the formed Pd NPs, Pd NRs, and bulk Pt for ORR as shown in Fig. 1c, the half-wave potential ($E_{1/2}$) obtained from Pd NRs shifts positively by 85 mV compared to that of Pd NPs and approaches that of bulk Pt catalyst. Figure 1d demonstrates that the kinetic current density (j_K) of the Pd NRs approaches that of bulk Pt and is 10-fold higher than that of the Pd NPs at +0.85 V (a practical operating potential of a PEMFC cathode). The superior ORR activity of Pd NRs was attributed to the exceptionally weak interaction between the exposed Pd(110) facet of Pd NRs and the adsorbed O atoms, which was confirmed by the CO stripping experiments and density functional theory (DFT) calculations. This study indicated that 1D Pd nanostructures could be an efficient and cost-effective cathodic electrocatalysts for PEMFCs.

By taking advantage of the higher activity offered by certain platinum alloys, Yan and coworkers [75] reported that unsupported PtPd nanotubes (PtPdNTs) exhibited much enhanced mass activity toward ORR as fuel cell cathode electrocatalysts. In the study, Pt and PtPd nanotubes were prepared through a galvanic replacement reaction between the pre-synthesized silver nanorods and Pt or Pd precursors. Figure 2 shows the SEM and TEM images of the as-synthesized PtPd NTs. It can be clearly seen that the PtPd NTs display uniform diameter (45 nm), wall thickness (7 nm), and length (10 μm). The ORR activity and durability test are shown in Fig. 3. From Fig. 3b, it can be seen that the half-wave potential of the PtPdNTs (0.851 V) is higher than that of the synthesized Pt nanotubes (PtNTs) (0.837 V), platinum black (0.817 V), and Pt/C (0.828 V). The shift to more positive potentials suggests clearly that the overpotential of ORR can be effectively reduced by using the bimetallic system. Moreover, the calculated mass- and specific-activity of the PtPd nanotubes are 1.4 and 1.8 times higher than those of the platinum black, respectively. Figure 3a shows the ECSA change with number of cyclic voltammetry (CV) cycles at three electrocatalysts. After 1000 cycles,
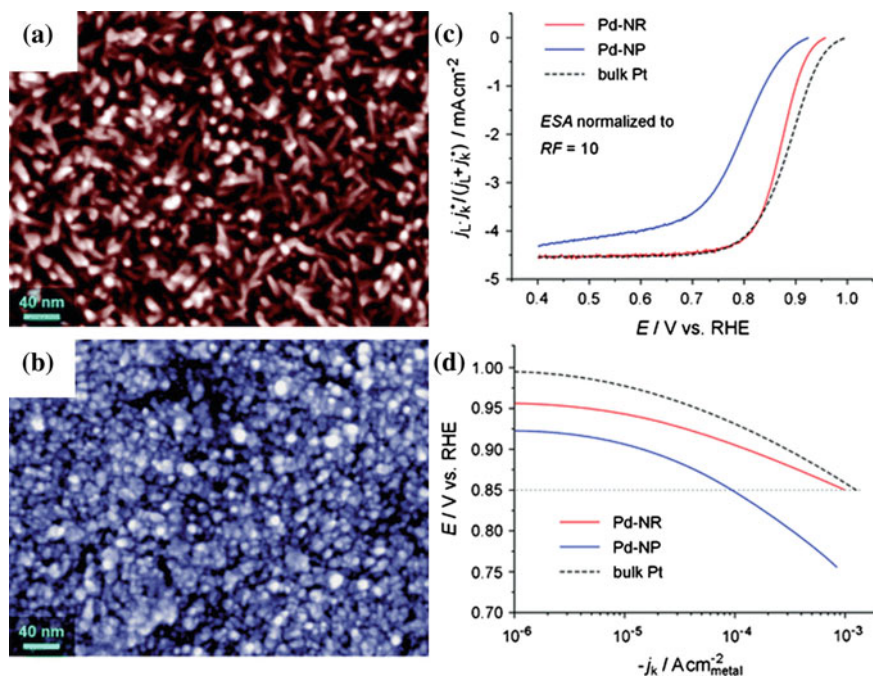
Fig. 1 SEM images of two typical morphologies of Pd obtained by adjusting the precursor concentration and deposition time: **a** Pd nanorods (Pd-NRs), 3×10^{-4} M PdCl$_2$, 100 s; **b** Pd nanoparticles (Pd-NPs), 1×10^{-5} M PdCl$_2$, 3000 s. ORR data for Pd-NR, Pd-NP, and bulk Pt, obtained in an O$_2$ saturated 0.1 M HClO$_4$ solution at a rotation rate of 900 rpm and a scanning rate of 10 mV s^{-1}. **c** Normalized ORR profiles and **d** Tafel plots. The diffusion limited current (j_L) has been normalized to the geometric surface area (GSA), while the kinetic current density (j_K*) has been normalized to an electrochemical surface area (ESA) corresponding to a roughness factor (RF) of 10. Reprinted from Ref. [44] with permission by the American Chemical Society
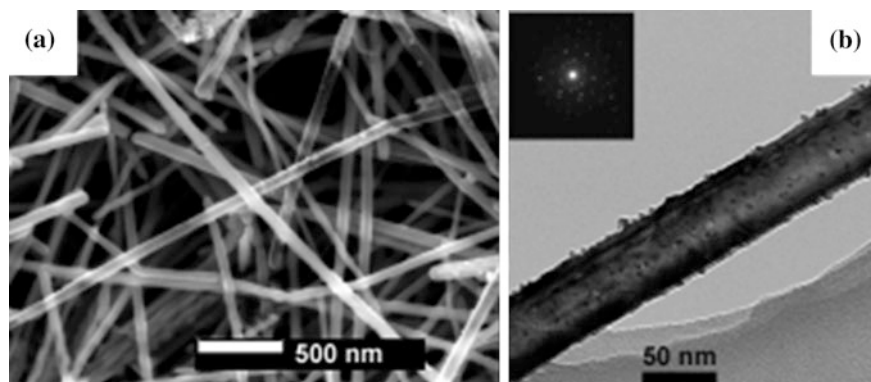

Fig. 2 **a** SEM image of PtPd nanotubes. **b** TEM image and electron diffraction pattern (*inset*) of the PtPd nanotubes. Reprinted from Ref. [75] with permission by Wiley-VCH

Fig. 3 a Loss of
electrochemical surface area
(ECSA) of Pt/C (E-TEK),
platinum-black (PtB;
E-TEK), and PtNT catalysts
with number of CV cycles in
Ar-purged 0.5 M H_2SO_4
solution at 60 °C (0–1.3 V
vs. RHE, sweep rate
50 mV s^{-1}). **b** ORR curves
(shown as current–voltage
relations) of Pt/C, platinum
black (PtB), PtNTs, and
PdPtNTs in O_2-saturated
0.5 M H_2SO_4 solution at
room temperature (1600 rpm,
sweep rate 5 mV s^{-1}). *Inset*
mass activity (*top*) and
specific activity (*bottom*) for
the four catalysts at 0.85 V.
Reprinted from Ref. [75]
with permission by Wiley-
VCH
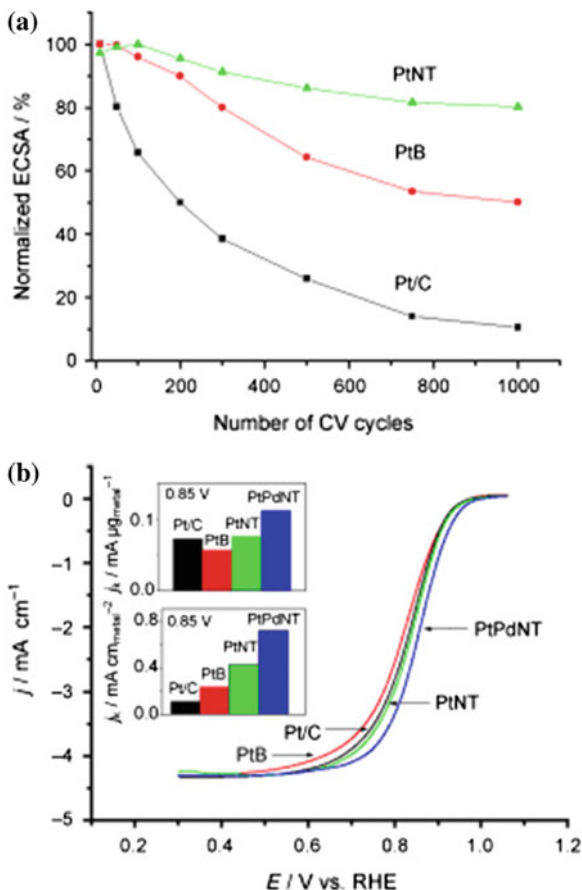
platinum-black and Pt/C catalysts lose about 51 and 90 % of their ECSA, respectively. However, the Pt nanotubes only lose about 20 % of its ECSA, indicating the enhanced electrochemical stability of the unsupported nanotubes. In addition, the durability tests indicated that the ECSA of PtPd NTs is 5.8 times higher than that of the Pt/C and 1.5 times higher than that of the Pt NTs. Such enhanced activity and durability of PtPd NTs toward ORR can be ascribed to the change of electronic structures induced by the addition of Pd into the platinum lattice.

The electrocatalytic results obtained from the Pt and PtPd nanotubes clearly indicated that the catalytic performance of 1D nanomaterials can be improved by decorating another metal. Recently, Alia et al. [79] synthesized Pt-coated Pd nanotubes (Pt/PdNTs) with a wall thickness of 6 nm, outer diameter of 60 nm, and length of 5–20 μm via the partial galvanic displacement of Pd nanotubes with Pt. ORR on Pt/PdNTs, Pt nanotubes (PtNTs), Pd nanotubes, and supported Pt nano-particle was studied to evaluate their electrocatalytic activities as PEMFCs

cathodes. It was found that the Pt/PdNTs with Pt loading of 9 wt% (PtPd 9) produced an ORR mass activity 95 % of PtNTs. Taking account of the reduction of Pt loading in PtPd 9, the Pt mass activity of Pt/PdNTs is actually significantly higher than PtNTs. Compared to the dollar activity target (9.7 A $^{-1}$) of the United States Department of Energy (DOE), the calculated dollar activity of PtPd 9 (10.4) exceeds that of DOE by 7 %. On the other hand, the area activity of Pt/PdNTs outperformed the DOE target by greater than 40 %.

In a recent paper, Koenigsmann et al. [97] reported the synthesis, characterization, and electrochemical performance of novel 1D ultrathin Pt monolayer shell-Pd nanowires core catalyst. They found that the UV ozone-treated nanowires exhibited outstanding area and mass specific activities of 0.77 mA cm^{-2} and 1.83 A mg$_{Pt}^{-1}$ toward ORR, respectively, which were significantly enhanced as compared with conventional commercial Pt nanoparticles, core-shell nanoparticles, and acid-treated nanowires. This study also indicated that the methods to remove the organic residue on the surface of nanomaterials can affect their subsequent catalytic activity. In another report by Koenigsmann et al. [66] they successfully synthesized a series of bimetallic Pd$_{1-x}$Au$_x$ and Pd$_{1-x}$Pt$_x$ nanowires with control over composition and size through an ambient, template-based technique. In their report, the as-synthesized 1D alloy nanowires (ANWs) maintain significantly enhanced activity toward ORR as compared with commercial Pt nanoparticles and other 1D nanostructures. Specifically, the Pd$_9$Au and Pd$_4$Pt nanowires possess ORR activities of 0.49 and 0.79 mA cm^{-2}, which are larger than the analogous value from commercial Pt nanoparticles (0.21 mA cm^{-2}).

Recent studies have demonstrated that Pd catalysts can produce high ORR activity when combined with appropriate transition metals, such as Co, Fe, Mo, etc [59, 61, 98]. By an organic phase reaction of [Pd(acac)$_2$] and thermal decomposition of [Fe(CO)$_5$] in a mixture of oleyamine and octadecene at 160 °C, Li et al. [73] synthesized PdFe nanorods (PdFe-NRs) with tunable length. The morphology of the PdFe products can be tuned by altering the volumetric ratio of oleyamine (OAm) and octadecene (ODE) surfactants during the synthesis. As shown in Fig. 4a, under the OAm/ODE ratio of 1/3, there is only PdFe nanoparticles formation with an average particle size of 2–4 nm. With the ratio increasing to 1/1, PdFe nanorods with a diameter of 3 nm and length of 10 nm were formed (Fig. 4b). If only OAm was used in the synthesis, long PdFe nanorods with a length of 10 nm can be produced. Interestingly, around 20–40 PdFe nanorods were self-assembled to "flower"-like bundles (Fig. 4c, d), and the distance between two nanorods is around 2–4 nm. It was proposed that this bundle structure is likely to form a thin and dense catalyst layer in a membrane-electrode assembly (MEA), which can facilitate the mass transport of reactants. In the following electrocatalytic investigations, the as-synthesized PdFe-NRs demonstrated a better PEMFC performance than commercial Pt/C in the practical working voltage region (0.80–0.65 V), which can be attributed to their unique 1D morphology, high intrinsic activity toward ORR, reduced cell inner resistance, and improved mass transport.
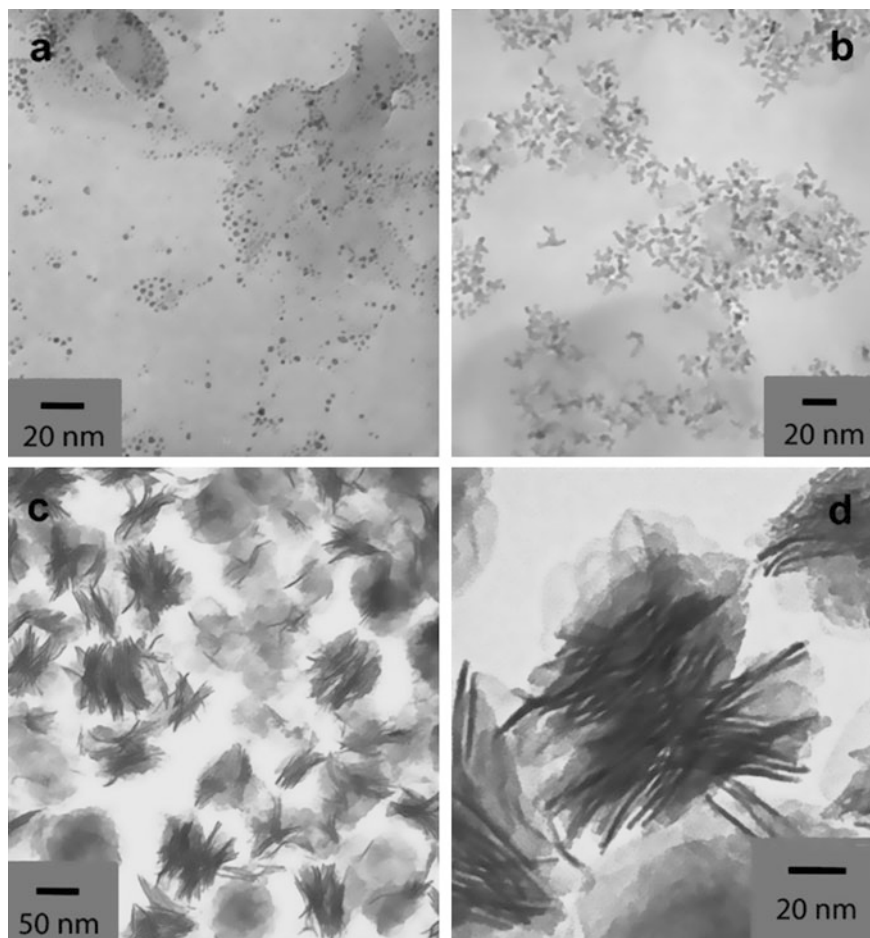
Fig. 4 TEM images of the PdFe nanoparticles (**a**) and nanorods with a length of 10 nm (**b**), 50 nm (**c**), and 50 nm in one bundle (**d**). Reprinted from Ref. [73] with permission by Elsevier

In another report, Li and co-workers [74] reported the preparation and characterization of PdFe nanoleaves (NLs) for ORR. The novel nanoleaf-structured materials were synthesized through a wet chemical reduction method with the presence of oleylamine, and the composition of the final products can be tuned by changing the precursors of $Pd(acac)_2$ and $Fe(CO)_5$. It was found that the Fe concentration largely affects the morphology of the as-synthesized nanostructures. From the TEM images shown in Fig. 5, the nanoleaves are actually composed of Fe-based nanosheets and Pd-rich nanowires embedded in the sheets. Lower Fe content results in the formation of 1D Pd nanowires with shorter lengths and larger diameters. The high resolution TEM (HRTEM) images in Fig. 5g shows that the side surfaces of these Pd-rich nanowires are composed of Pd(111) planes, while
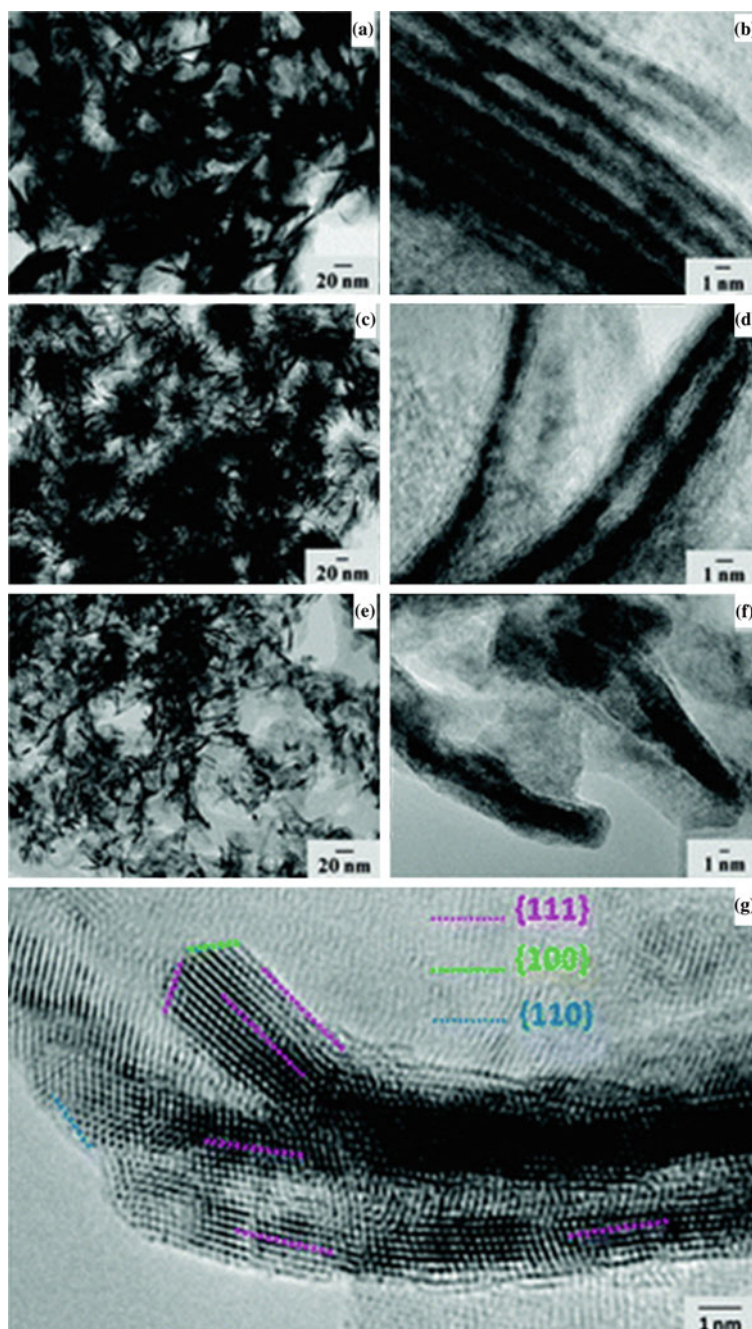
Fig. 5 TEM images of the Pd_xFe_y nanoleaves (NLs): **a**, **b** Pd_1Fe_1-NL, **c**, **d** Pd_2Fe_1-NL, **e**, **f** Pd_5Fe_1-NL, and **g** HRTEM image of Pd_1Fe_1-NL. Reprinted from Ref. [74] with permission by the American Chemical Society

Fig. 6 ORR polarization curves of commercial Pt/C (*black curve*), Pd/C (self-prepared by EG method, *red curve*), Pd₁-NL/C (*green curve*), and Pd₂-NL/C (*blue curve*) in oxygen saturated 0.1 M NaOH (conditions: 10 mV s⁻¹, 2500 rpm, and room temperature). Reprinted from Ref. [74] with permission by the American Chemical Society
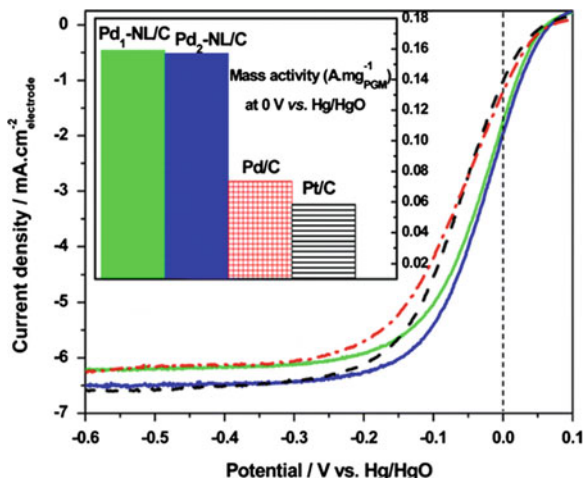
the tips and ends are predominated by Pd(110) and Pd(100) facets. The morphology of PdFe-NLs is distinctively different from the Pd nanorods with larger diameter (5–10 nm) prepared using PVP as a stabilizer. The varied Pd nanostructures suggest that the different synthesis conditions, i.e., different surfactants, presence/absence of Fe, etc., can affect the growth mechanisms of 1D nanomaterials. By etching away the enveloping Fe-rich sheets using an organic acid, the Pd-rich NWs are exposed on the surfaces of the nanoleaves, and they demonstrated high reactivity toward electrocatalytic reduction of oxygen in a 0.1 M NaOH electrolyte. The ORR polarization curves obtained from different catalysts are shown in Fig. 6. It can be observed that the Pd-NLs show a remarkable improvement in ORR activity with the half-wave potential shifting positively by $\sim$38 mV, compared to commercial Pt/C catalyst. Moreover, the mass activity of Pd₁-NL and Pd₂-NL are 0.159 and 0.157 A mg_{Pd}^{-1}, respectively, which are twice higher than that of Pd/C (0.0735 A mg_{Pd}^{-1}) and $\sim$2.7 times higher than that of Pt/C (0.0585 A mg_{Pt}^{-1}) at 0 V versus Hg/HgO. For the specific activity, the Pd₁-NLs and Pd₂-NLs at 0 V are 312 and 305 $\mu A\ cm_{Pd}^{-2}$, respectively, which are higher than that of Pd/C (207 $\mu A\ cm_{Pd}^{-2}$) and Pt/C (103 $\mu A\ cm_{Pt}^{-2}$). The enhanced electrocatalytic activity of Pd NLs may be attributed to the unique nanoleave structure, which provides more Pd(111) facets, a large surface area, and more resistance to oxide formation.

More recently, Xu et al. [77] prepared a novel PdCu bimetallic nanotubes with hierarchically hollow structures via a galvanic displacement reaction by using dealloyed nanoporous copper as both a template and reducing agent and found that the PdCu nanocomposites exhibit enhanced ORR activity. In this study, three-dimensional nanoporous copper (Fig. 7a, b) was firstly synthesized by dealloying Cu/Al alloy foils in NaOH. PdCu bimetallic hollow structures were then produced through a galvanic replacement reaction between nanoporous copper and K₂PdCl₄. The SEM and TEM measurements (Fig. 7c–f) show that the
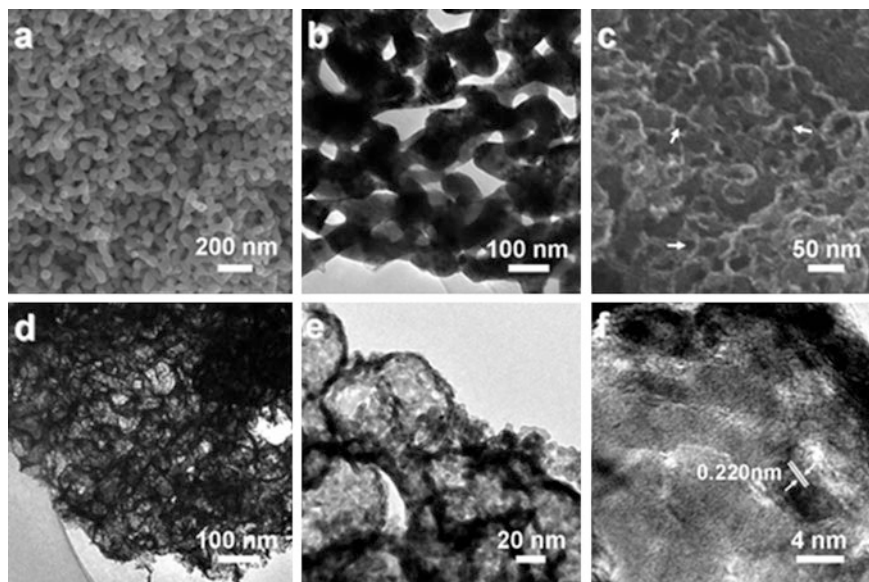
Fig. 7 SEM and TEM (HRTEM) images of nanoporous copper (**a**, **b**) and nanotubular mesoporous PdCu bimetallic nanostructure (**c–f**), respectively. Reprinted from Ref. [77] with permission by the American Chemical Society

formed PdCu bimetallic nanocomposites display nanotubular mesoporous nanostructures. The electrochemical polarization curves of the nanotubular mesoporous PdCu (NM-PdCu) revealed that the half-wave potential of the NM-PdCu for ORR was 0.840 V, which was 60 mV more positive than that of the commercial Pd/C catalysts. Moreover, the NM-PdCu catalyst is also superior to the commercial Pt/C (0.825 V) catalyst with more positive half-wave potential. The calculated specific activity of NM-PdCu at 0.8 and 0.85 V is 1.5 and 1.4 times that of the Pt/C catalyst at the respective potentials. From the Koutecky-Levich curves in rotating disk voltammetry measurements, a nearly complete reduction of O_2 to H_2O on the NM-PdCu surface via an efficient four-electron reaction process was obtained. More importantly, based on the experimental results, NM-PdCu catalyst showed enhanced methanol tolerance as compared with the commercial Pt/C and Pd/C catalysts. The enhanced ORR activity, stability, and methanol tolerance were ascribed to the presence of sublayer Cu atoms, which provide an electronic modification for the topmost Pd layer by a surface strain effect or an alloying effect. This effect could provide unique surface sites for the adsorption of O_2 molecules and be beneficial for their subsequent electro-reduction. Furthermore, the unique three-dimensional bicontinuous spongy structure and various hollow channels provide good transport channels for medium molecules and electrons, which may greatly facilitate the reaction kinetics of ORR on the catalytic surfaces.

3 One-Dimensional Pd-Based Nanomaterials as Effective Anode Electrocatalysts

3.1 Electrocatalysts for Alcohol Oxidation

Although Pt-based alloy catalysts, especially nanostructured PtRu, have been widely used as anode electrocatalysts in DMFC, the effectiveness and wide application of these catalysts are still largely limited due to their relatively low electrochemical stability and low tolerance to CO poisoning [99]. To address the disadvantages suffered from Pt-based catalysts, recent efforts have been devoted to the development of more efficient catalysts with high stability and high CO-tolerance. Recently, Pd-based nanomaterials have been found to exhibit high CO tolerance and superior electrocatalytic activity toward CO oxidation [38, 100], methanol oxidation [101, 102], and ethanol oxidation [69]. However, there are still obstacles in utilizing Pd nanoparticles because they often experience irreversible aggregation during electrocatalytic cycles, leading to a significant loss of catalytic activity and durability. Thus, 1D Pd-based nanomaterials have emerged as a potential electrocatalysts owing to their unique anisotropic structure. In particular, the ordered surface structure of one-dimensional nanostructured catalysts could affect the electrochemical and electrocatalytic properties. Among various synthetic approaches for one-dimensional nanostructure arrays, an anodic aluminum oxide (AAO) membrane-based method has received increasing attention because its uniform and reproducible porous structure as an ideal template can produce highly ordered nanotube or nanowire-type arrays.

Cheng et al. [71] prepared highly ordered Pd nanowire arrays (NWAs) using a porous AAO template by pulse electrodeposition method. It can be clearly observed from Fig. 8b–d that the Pd nanowires templated by AAO are highly ordered with uniform diameters of about 50 nm and length of 850 nm. Meanwhile, the as-prepared Pd NWAs retain the size and near cylinder shape of the pores of the AAO template as shown in Fig. 8a. More interestingly, the as-synthesized Pd NWAs exhibit good electrocatalytic activity toward isopropanol and methanol oxidation at room temperature. By using a similar AAO template-electrodepositon method and a subsequently magnetron sputtering techniques, Cheng's group also prepared highly ordered Pd/Pt core-shell nanowire arrays (Pd/Pt NWAs) [72]. In the method, Pd NWAs were first synthesized in AAO template. After removing the template in NaOH solution, Pt film was then coated on the surface of Pd NWAs through magnetron sputtering. Figure 9 shows the SEM images of the as-synthesized Pd and Pd/Pt NWAs. By using AAO as template, highly ordered Pd NWAs with smooth surface and uniform diameter and length were produced. However, after magnetron sputtering of Pt, the surface of Pd nanowires was covered by a thin layer (~ 1.7 nm) of cotton-like aggregated Pt nanoparticles. Nevertheless, the microstructure and morphology of Pt coated Pd NWAs is more or less the same as original Pd NWA core. Figure 10a shows the CVs of different electrodes in a nitrogen- saturated 0.5 M H_2SO_4 solution without methanol. It was found that the electrochemical active area
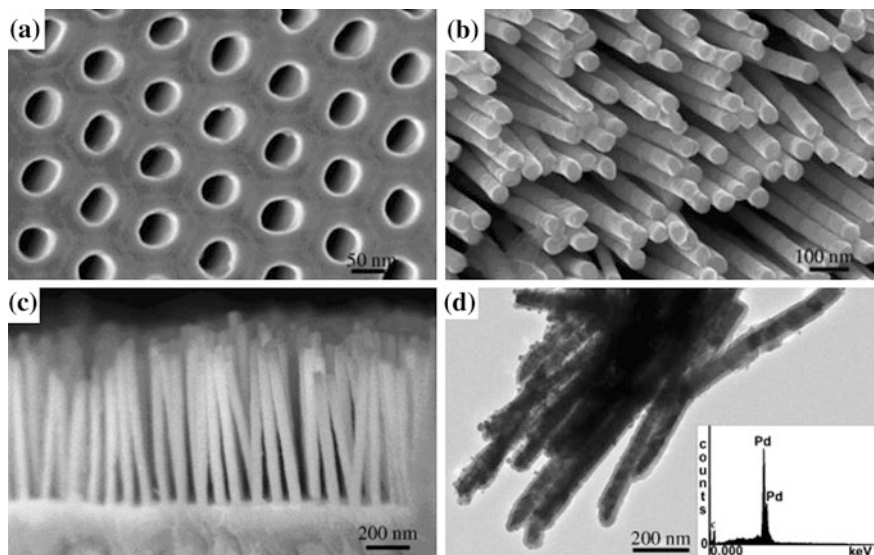
Fig. 8 Typical SEM images of **a** AAO template, **b** surface of Pd nanowire arrays (NWAs) with the diameter of 50 nm, **c** cross-section of Pd NWAs and **d** TEM image and EDX (*inset*) of Pd NWAs. Reprinted from Ref. [71] with permission by Elsevier

(EAA) of Pd/Pt core-shell NWAs electrode is 51 and 20 times larger than that of Pt thin film and PtRu/C electrode, respectively. This extremely high EAA from Pd/Pt core-shell NWAs shows that Pd/Pt core-shell NWAs nanostructure can substantially increase the effective electrochemical active sites most likely due to the very high surface-to-volume ratio of the highly ordered NWA core nanostructure and the high roughness of the Pt shell. By comparing the CVs in Fig. 10b, the Pd/Pt core-shell NWAs exhibit superior performance for methanol oxidation. It can be seen that the onset oxidation potential on Pd/Pt core-shell NWAs (0.19 V vs. SCE) is more negative than those on PtRu/C (0.21 V) and Pt thin film (0.39 V). The electrocatalytic activity, as measured by the peak current density in the forward scan is 22.7 mA cm^{-2} for the Pd/Pt core-shell NWAs, which is nearly 4.2 and 8.7 times higher than that of the E-TEK PtRu/C and Pt thin film electrodes. On the other hand, the peak potential for methanol oxidation on the Pd/Pt core-shell NWAs electrode is 170 mV more negative than that on the conventional PtRu/C electrode, indicating the enhanced electrode kinetics. Moreover, the Pt mass specific current peak density is 756.7 mA mg$_{Pt}^{-1}$ for the Pd/Pt core-shell NWAs electrode, which is four times higher than the E-TEK PtRu/C electrode (180.0 mA mg$_{Pt}^{-1}$). Since Pd is electrocatalytically inactive in acidic media, the high EAA and mass specific current for methanol oxidation can be mainly attributed to the Pt shell sputtered on the surface of Pd NWAs core.
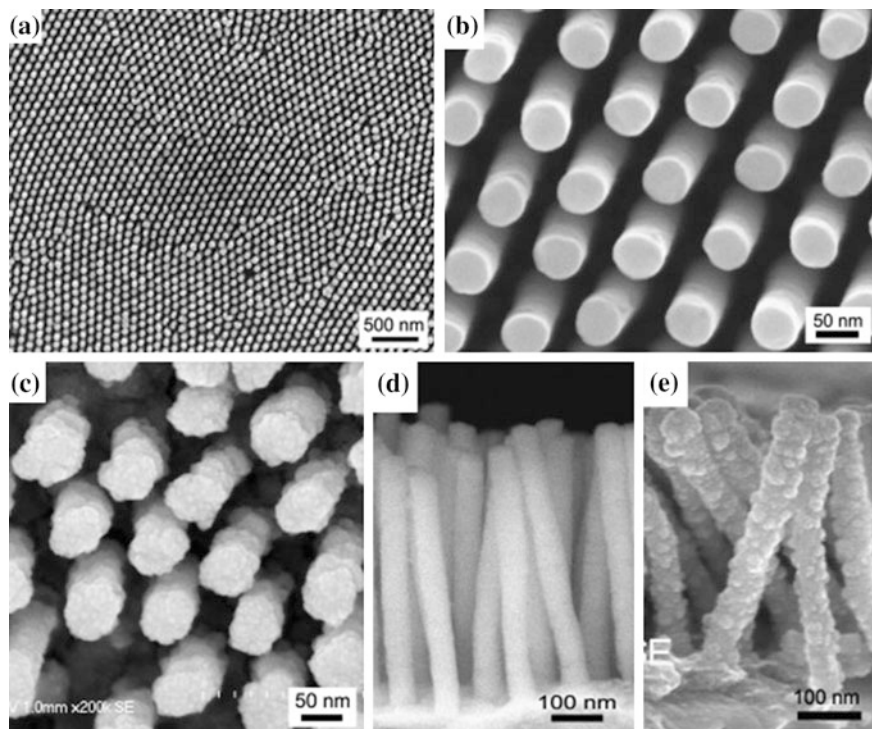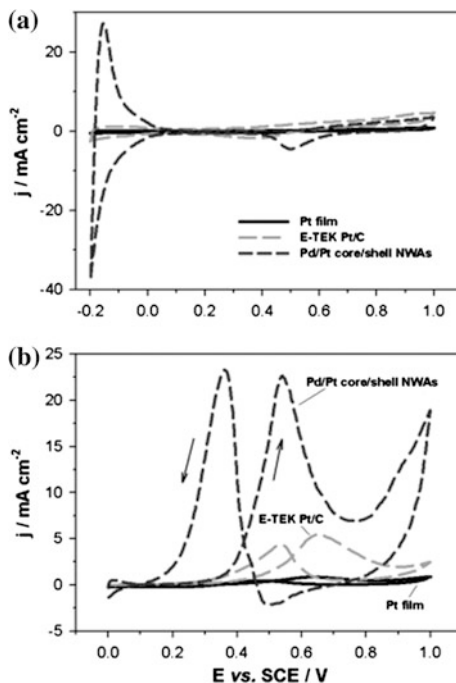
Fig. 9 SEM micrographs of **a** and **b** surface of Pd NWAs, **c** surface of Pd/Pt core-shell NWAs, **d** cross-section of Pd NWAs, and **e** cross-section of Pd/Pt core-shell NWAs. Reprinted from Ref. [72] with permission by Elsevier

Earlier studies have shown that 1D NWs have a strong interaction with carbon supports and are less vulnerable than conventional nanoparticles to dissolution, Ostwald ripening, and aggregation in strong acidic electrocatalytic conditions [71, 103]. Different from the bimetallic Pd-based alloys, Guo et al. [104] recently synthesized ultrathin (2.5 nm) trimetallic FePtPd alloy nanowires (NWs) with tunable compositions and controlled length (less than 100 nm). These FePtPd NWs exhibited composition-dependent catalytic activity and stability for methanol oxidation reaction. As shown in Fig. 11a, the as-prepared $Fe_{28}Pt_{38}Pd_{34}$ NWs exhibit the highest catalytic activity for methanol oxidation with the mass current density of 488.7 mA mg_{Pt}^{-1} and peak potential decreased from 0.665 V (vs. Ag/AgCl) obtained on Pt nanoparticle catalysts to 0.614 V. More interestingly, the $Fe_{28}Pt_{38}Pd_{34}$ displayed enhanced electrochemical stability with the mass current density (98.1 mA mg_{Pt}^{-1}) after i-t test for 2 h at 0.4 V (Fig. 11b). Figure 11c, d indicates that there was almost no noticeable morphology change before and after i-t tests, whereas the Pt nanoparticles experienced substantial aggregation. The authors attributed the enhanced stability of NWs versus NPs to the stronger NW interactions with carbon support and/or by better NW structure stability, which

makes the NWs less subject to dissolution, Ostwald ripening, and aggregation in acidic solution.

Compared to methanol, ethanol is less toxic and can be produced in large quantities from agricultural products. Moreover, ethanol is the major renewable biofuel from the fermentation of biomass. Recent studies have shown that Pd-based nanomaterials are electrocatalytically active for ethanol oxidation in alkaline medium, representing an important alternative to Pt-based catalysts for direct ethanol AFCs [69, 80, 105]. For instance, Jiang and coworkers [69] successfully synthesized highly ordered Pd nanowires arrays (Pd NWA) through the anodized aluminum oxide (AAO) template-electrodeposition method. The SEM characterizations in Fig. 12 show that the as-synthesized Pd NWAs after AAO template fully dissolved are highly ordered with uniform diameter *ca.* 80 nm and length *ca.* 800 nm. The uniform porous structure of the nanowires can effectively improve their ECSA and thus enhance the active sites for the electrocatalytic reaction. Electrochemical experiments demonstrated that the as-synthesized Pd NWA exhibited excellent electrocatalytic activity and stability for ethanol oxidation in alkaline media compared to the conventional Pd film electrodes and the well-established commercial E-TEK PtRu/C electrocatalysts. As can be seen from Fig. 13, the onset potential for the ethanol oxidation on the Pd NWA electrode is −0.62 V, which is 150 mV more negative than the −0.45 V observed on the Pd film electrode and 40 mV more negative than the −0.58 V obtained from the conventional E-TEK PtRu/C
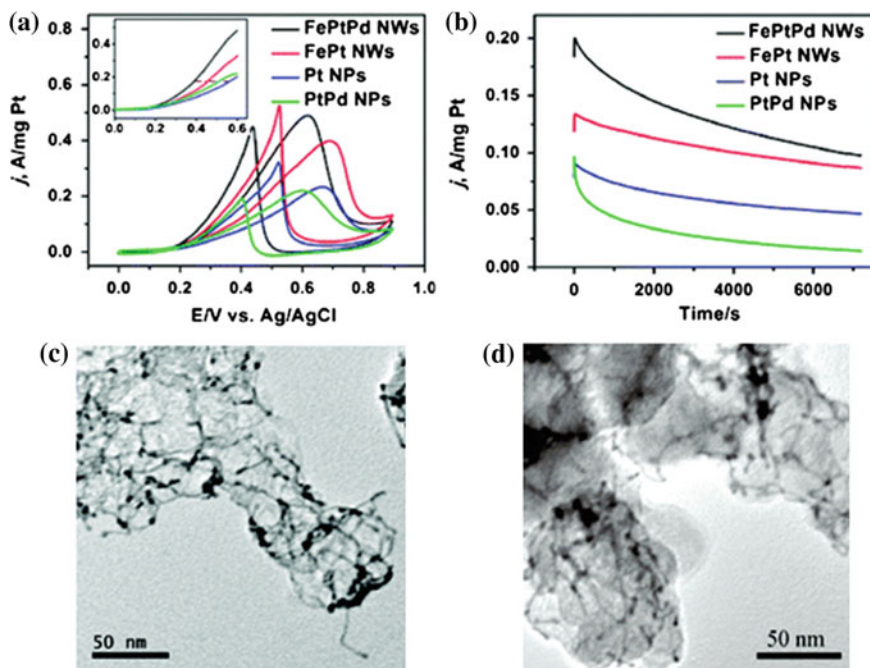
Fig. 11 CVs (**a**), linear sweep voltammetry (*inset*) and i-t *curves* (**b**) of methanol oxidation reaction catalyzed by $Fe_{28}Pt_{38}Pd_{34}$ NWs, FePt NWs, Pt NPs and PtPd NPs in 0.1 M $HClO_4$ + 0.2 M methanol solution. The CVs were obtained at a scan rate of 50 mV s^{-1} and the i-t *curves* were collected at a constant potential of 0.4 V. TEM images of the $Fe_{28}Pt_{38}Pd_{34}$ NWs/C before (**c**) and after (**d**) 2 h i-t test. Reprinted from Ref. [104] with permission by the American Chemical Society
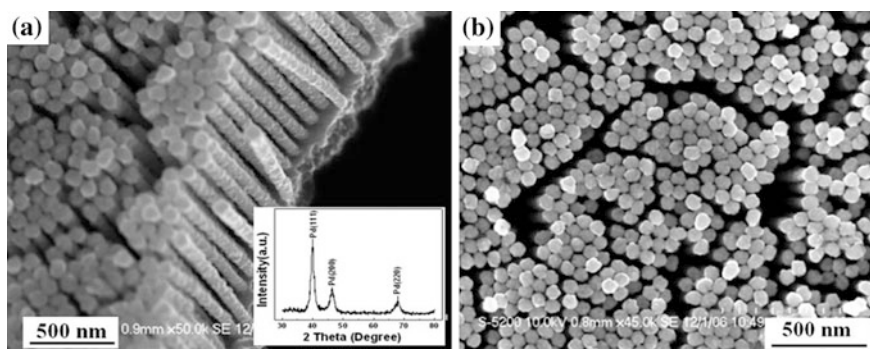

Fig. 12 SEM images of **a** cross section and **b** surface of Pd NWAs. *Inset* in (**a**): XRD pattern of Pd NWAs. Reprinted from Ref. [69] with permission by Wiley-VCH

Fig. 13 CVs measured on a Pd film electrode (*curves a*, Pd loading: 1.1 mg cm^{-2}), E-TEK PtRu (2:1 by weight)/C electrode (*curves b*, Pt loading: 0.24 mg cm^{-2}), and Pd NWA electrode (*curves c*, Pd loading: 0.24 mg cm^{-2}) in 1.0 M KOH + 1.0 M C$_2$H$_5$OH (*upper panel*) and 1.0 M KOH (*lower panel*) solution at a scan rate of 50 mV s^{-1}. Reprinted from Ref. [69] with permission by Wiley-VCH
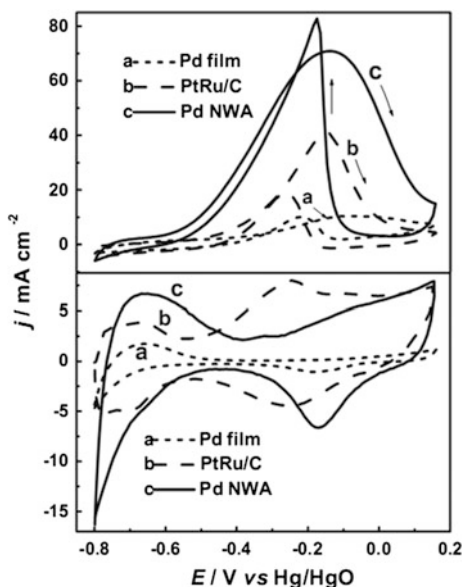
electrocatalyst. The negative shift of onset potential indicates the significant enhancement in the kinetics of the ethanol oxidation reaction on Pd NWAs. Similarly to methanol oxidation on Pt-based electrocatalysts in acid media, ethanol oxidation on Pd NWA electrode is also characterized by well-separated anodic peaks in the forward and reverse scans. The anodic peak current density on the Pd NWA electrode is seven times of that on the Pd film electrode and almost twice of that on the PtRu/C electrode. The obtained electrochemical results indicate that the 1D Pd NWA nanomaterials could be an efficient anode electrocatalysts for direct ethanol AFCs.

Interface formed in a bimetallic system plays an important role in the catalytic promotional effect and studies on bimetallic interface are also critical to investigate the fundamental mechanism of enhanced electrocatalytic activity for fuels oxidation. Recently, Yu et al. [80] designed unsupported Pd–Au bimetallic tubular nanostructures through one-step nonaqueous solvent electrodeposition method and studied their catalytic activity for electrooxidation of ethanol. With the electrodeposition method, tubular, dispersed, and unsupported Pd–Au bimetallic heterostructure tubes (BHTs) were formed with controlled atom percentage of Pd and with several micrometer-sized lengths as measured by SEM (Fig. 14a, b). The TEM image in Fig. 14c indicates the uniform wall thickness of the nanotubes, composed of many flocky-like spheres. Moreover, the unique porous structure of the BHTs could promote the mass transfer and effectively expose their inner and outer surfaces. From the HRTEM images shown in Fig. 14d–f, the single Au nanoparticle and the interfaces of Au–Pd and Au–Au can be observed clearly. The resultant tubular materials demonstrated high surface area, high stability, and
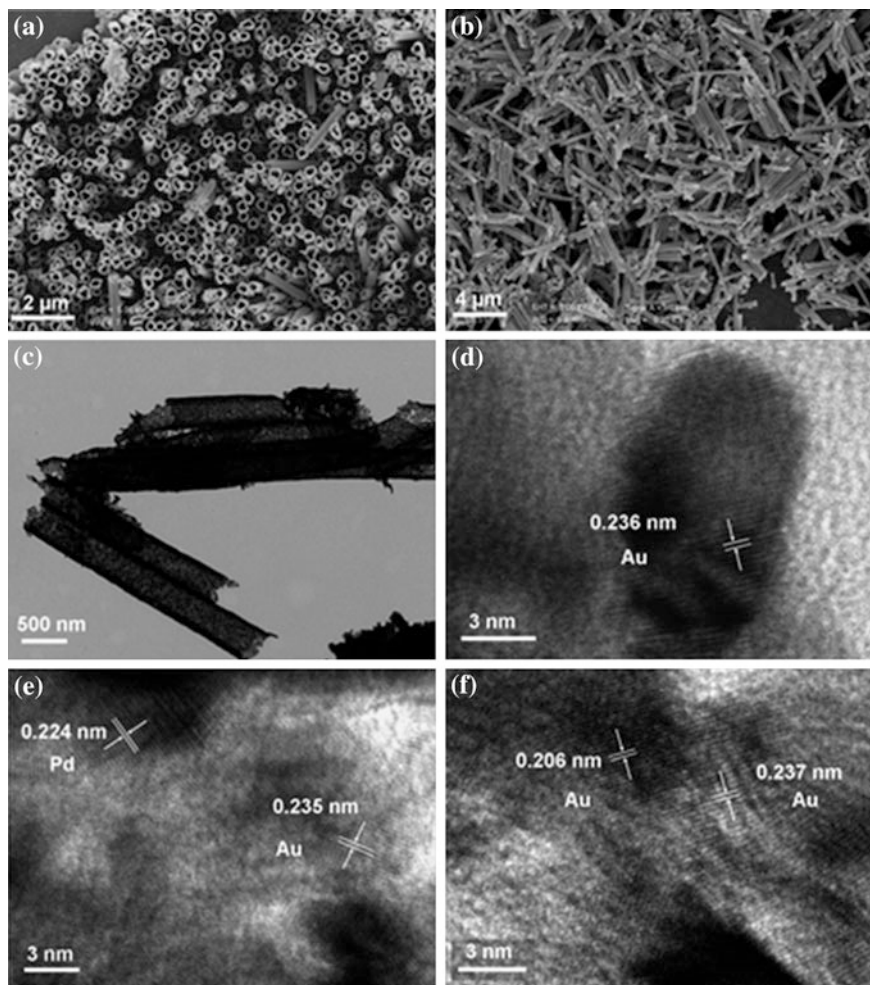
Fig. 14 **a**, **b** SEM images of Pd–Au bimetallic heterostructure tubes (BHTs). **c** TEM image of unsupported Pd-Au BHTs. HRTEM images of **d** a single particle **e** overlapped Pd–Au particles near the edge of the pore area, and **f** Au–Au particle interface, respectively. Reprinted from Ref. [80] with permission by the American Chemical Society

durability during the electrocatalytic studies. Figure 15 shows the CVs of various catalysts supported on glassy carbon electrode (GCE) in N_2-purged 1.0 M KOH aqueous solution with ethanol at a sweep rate of 50 mV s^{-1}. By comparison with Au nanotubes, Pd nanotubes, and commercial Pt/C catalysts, the synthesized Pd–Au BHTs exhibited larger ECSA (Fig. 15a), higher pseudo-area and mass activities (Fig. 15b–e), and higher electrochemical stability (Fig. 15f), suggesting that they can act as efficient Pt-free catalysts for fuel cells or other applications. The enhanced electrocatalytic performance was attributed to the electronic structure,
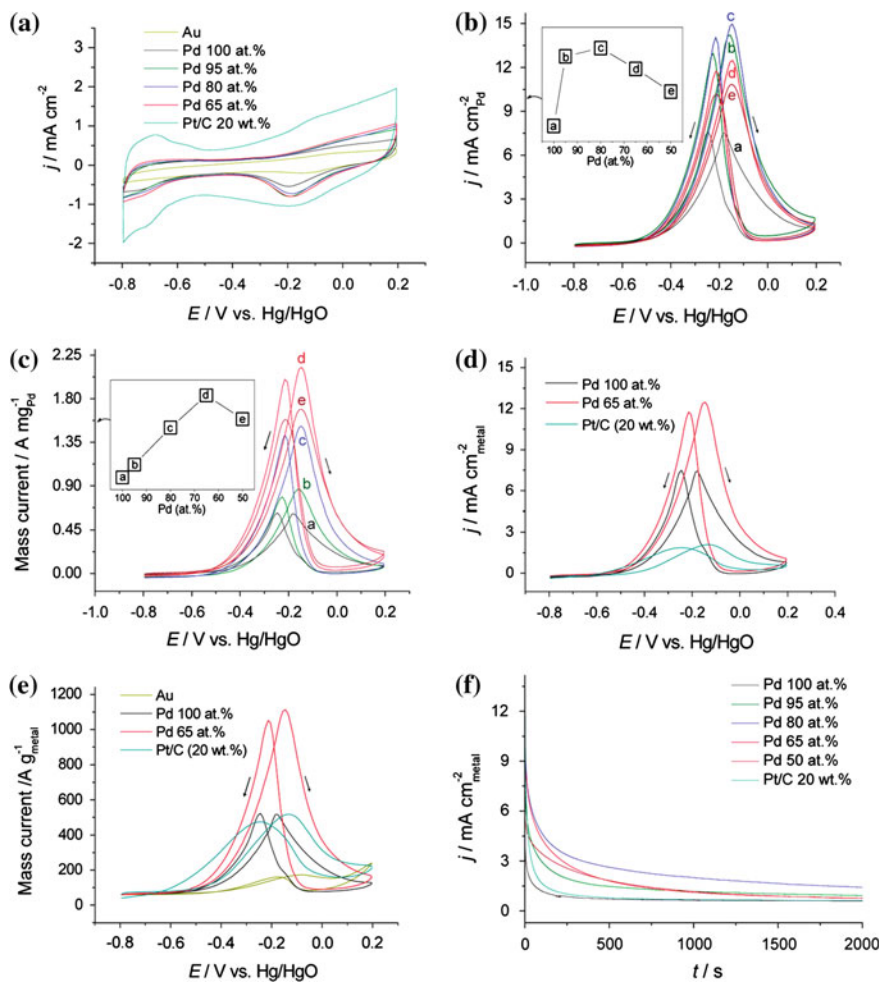
Fig. 15 Cyclic voltammograms (CVs) for determining the relative ECSA change of Pd and electrocatalytic activity. **a** CVs recorded in a N_2-purged 1.0 M KOH solution at room temperature. Pseudo-area activity (**b**) and mass activity (**c**) of unsupported Pd–Au BHTs with different Pd atom percentage for ethanol oxidation in 1.0 M KOH + 1.0 M C_2H_5OH. The *insets* show the peak current variation by increasing the Au atom percentage. **d** Pseudo-area activity and **e** mass activity of Pd NP tubes, unsupported Pd–Au BHTs, and Pt/C catalyst. **f** Chronoamperometric curves for ethanol electrooxidation at −0.3 V versus Hg/HgO on Pd NP tubes, unsupported Pd–Au BHTs, and Pt/C catalyst. Scan rate: 50 mV s^{-1}. Reprinted from Ref. [80] with permission by the American Chemical Society

local reactivity, and the significant coupling of d orbitals at the Pd–Au particle interfaces [80, 106].

More recently, Zhu et al. [64] developed a facile and general approach to synthesize high aspect ratio 1D Pd-based ANWs and found that the as-prepared
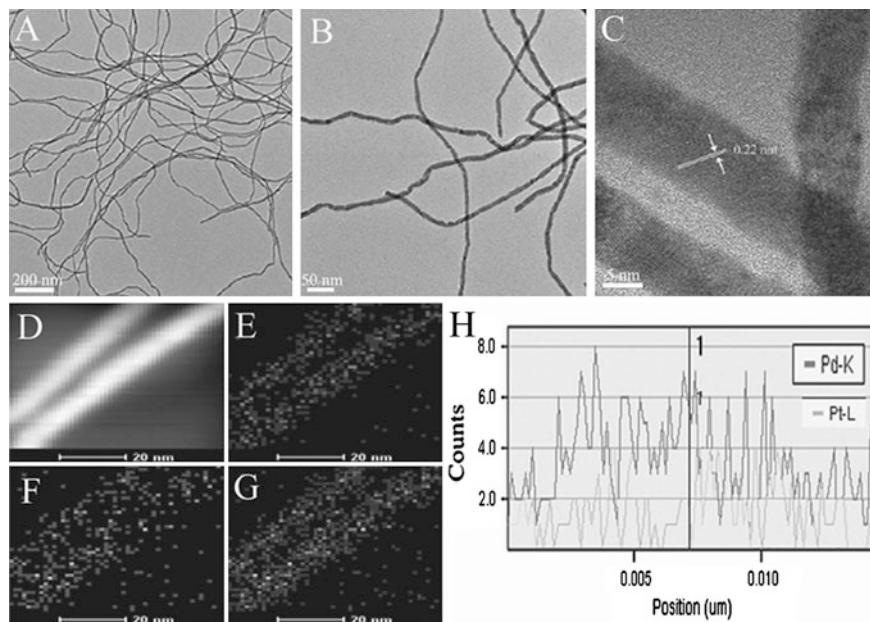
Fig. 16 TEM (**a**, **b**) and HRTEM (**c**) images of the obtained $Pd_{80}Pt_{20}$ nanowires. HAADF-STEM-EDS mapping images (**d**–**g**) of $Pd_{80}Pt_{20}$ nanowires. The cross-sectional compositional line profiles of individual $Pd_{80}Pt_{20}$ nanowire (**h**). **e** Pd-K; **f** Pt-L; **g** Pd-K + Pt-L. Reprinted from Ref. [64] with permission by Wiley-VCH

PdPt ANWs exhibit significantly enhanced activity and stability toward ethanol oxidation in alkaline medium. Figure 16a and b show the TEM images of the $Pd_{80}Pt_{20}$ ANWs templated from pre-synthesized Te NWs under different magnifications, clearly indicating the formation of uniform nanowires with high aspect ratios, an average diameter of 10.8 nm, and lengths up to tens of micrometers. HRTEM and elemental mapping measurements (Fig. 16c–h) revealed that both Pd and Pt elements are homogeneously distributed without significant segregation of each component. Electrochemical experiments are then performed to evaluate the catalytic activity of the PdPt ANWs toward alcohol oxidation. As shown in Fig. 17a, for the PdPt ANWs with different compositions, the $Pd_{45}Pt_{55}$ ANWs displays the highest activity toward ethanol oxidation in terms of onset potential and peak current. Based on the CV comparison in Fig. 17b, the mass activities on the $Pd_{45}Pt_{55}$ ANWs modified electrode is about 1.2 and 1.8 times of those on the Pd NWs and Pt nanotubes electrodes for ethanol oxidation. Moreover, the $Pd_{45}Pt_{55}$ ANWs also show a higher activity than commercial Pd/C electrocatalyst for ethanol oxidation. From the current–time curves recorded at −0.2 V shown in Fig. 17c, the $Pd_{45}Pt_{55}$ ANWs exhibit the highest catalytic stability among the studied electrocatalysts. On the other hand, the as-prepared 1D $Pd_{45}Pt_{55}$ catalyst also shows higher electrocatalytic activity and stability compared to the
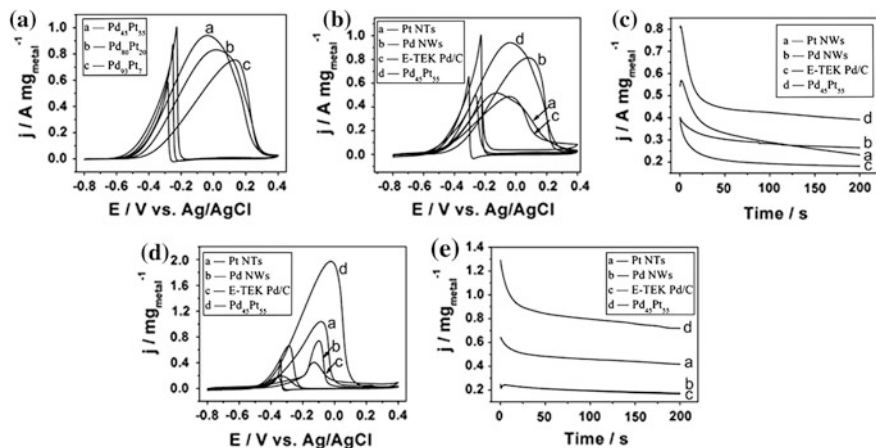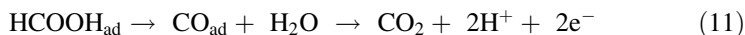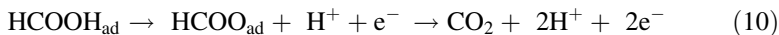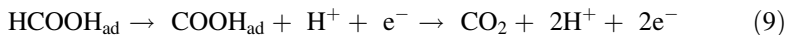
Fig. 17 **a** CVs of the Pd_xPt_y electrodes in a 0.5 M NaOH + 1 M ethanol solution; **b** CVs of the $Pd_{45}Pt_{55}$, Pd NWs, Pt NTs and E-TEK Pd/C electrodes in a 0.5 M NaOH + 1 M ethanol solution; **c** Current density–time curves of the $Pd_{45}Pt_{55}$, Pd NWs, Pt NTs and E-TEK Pd/C electrodes in a 0.5 M NaOH + 1 M ethanol solution at −0.2 V; **d** CVs of the $Pd_{45}Pt_{55}$, Pd NWs, Pt NTs and E-TEK Pd/C electrodes in a 1 M KOH + 1 M methanol solution; **e** Current density–time curves of the $Pd_{45}Pt_{55}$, Pd NWs, Pt NTs and E-TEK Pd/C electrodes in a 1 M KOH + 1 M methanol solution at −0.2 V. The loading amount of noble metal is 71.4 μg cm^{-2} for each catalyst and all the potential scan rates are 50 mV s^{-1}. Reprinted from Ref. [64] with permission by Wiley-VCH

monometallic catalysts Pt NTs and Pd NWs and the commercial E-TEK Pd/C catalyst toward methanol oxidation in alkaline conditions (Fig. 17d, e). The excellent catalytic performance of the PdPt nanowires could be attributed to three aspects: (1) the high aspect ratio; (2) the electronic effect; and (3) the synergistic effect [64].

3.2 Electrocatalysts for Formic Acid Oxidation

Except for alcohol, formic acid is another potential fuel for liquid fuel cells. Formic acid is a liquid at room temperature and dilute formic acid is on the US Food and Drug Administration list of food additives. Although the energy density of formic acid is lower than that of methanol, formic acid can be oxidized at less positive potential and with faster kinetics than methanol at room temperature. Moreover, formic acid can be easily handled and stored, and the low crossover through the polymer membranes allows fuel cells to work at relatively high concentrations of fuel and thin membranes. Therefore direct formic acid fuel cells (DFAFCs) have attracted increasing attention in recent years. Three possible reaction paths of formic acid oxidation have been widely accepted [107–110].

$$HCOOH_{ad} \rightarrow \ COOH_{ad} + \ H^+ + \ e^- \rightarrow \ CO_2 + \ 2H^+ + \ 2e^- \qquad (9)$$

$$HCOOH_{ad} \rightarrow \ HCOO_{ad} + \ H^+ + e^- \rightarrow CO_2 + \ 2H^+ + \ 2e^- \qquad (10)$$

$$HCOOH_{ad} \rightarrow \ CO_{ad} + \ H_2O \ \rightarrow \ CO_2 + \ 2H^+ + \ 2e^- \qquad (11)$$

In the first and second paths, through dehydrogenation with forming different intermediates formic acid can be oxidized to CO_2 directly. The Eq. (11) represents the indirect pathway, in which the produced CO intermediate can adsorb strongly on the surface of catalyst, leading to the poisoning of catalyst. To overcome the heavy CO-poisoning and high-cost of Pt-based catalysts, recent extensive research efforts have been devoted to the development of non-platinum anode electrocatalysts. Recent studies, including in situ spectroelectrochemical studies showed that Pd-based catalysts can catalyze the oxidation of formic acid at the anode of PEMFCs with greater resistance to CO than Pt catalysts [42, 111].

Recently, we successfully synthesized nanoneedle-covered 1D palladium-silver nanotubes through a galvanic displacement reaction with Ag nanorods at 100 °C (PdAg-100) and room temperature (PdAg-25) [76]. TEM and SEM measurements displayed that the synthesized PdAg nanotubes exhibit a hollow structure with a nanoneedle-covered surface, which provide the perfect large surface area for catalytic applications. From the HRTEM images of PdAg-25 shown in Fig. 18a, b, the surface of the PdAg-25 nanotubes is decorated with crystalline Pd nanoparticles with Pd(111) planes, and meanwhile, Ag and AgCl particles are dispersed in the inner space of the nanotubes. From the elemental mapping and cross-sectional line profiles shown in Fig. 18d–g, silver is dispersed in the core and Pd mainly distributes on the shell of the nanotubes. From the CVs in 0.1 M $HClO_4$ solution in Fig. 19a, more charge for hydrogen desorption was obtained with PdAg-25 nanotubes compared with that of PdAg-100 with the same loading on electrode surface, indicating rougher surface and thus larger ECSA of PdAg-25 nanotubes. By comparing the CV curves of the electrodes in 0.1 M $HClO_4$ + 0.5 M HCOOH solution (Fig. 19b), one can see that the PdAg-100 nanotubes exhibit more negative anodic peak potential (+0.285 vs. +0.316 V) and much larger anodic peak current density (3.82 vs. 1.97 mA cm^{-2}) of formic acid oxidation than those of PdAg-25 under same conditions. The higher electrocatalytic activity of PdAg-100 nanotubes possibly as the consequences of the higher ratio of Pd to Ag (36:64) in PdAg-100 compared with that in PdAg-25 (25:75) and the annealing process of the nanotube surface structures at 100 °C. Chronoamperometric analyses (Fig. 19c–e) were carried out to evaluate the activity and stability of the PdAg nanotubes for formic acid electrooxidation. It can be seen that at the three studied potentials, the maximum initial and steady-state oxidation current densities obtained from both of the PdAg nanotubes are much larger than that from the bulk Pd electrode over the entire time period. On the other hand, the initial current density on the bulk Pd electrode decays much more rapidly than those of the as-synthesized PdAg nanotubes. These results indicate that the synthesized PdAg nanotubes exhibit
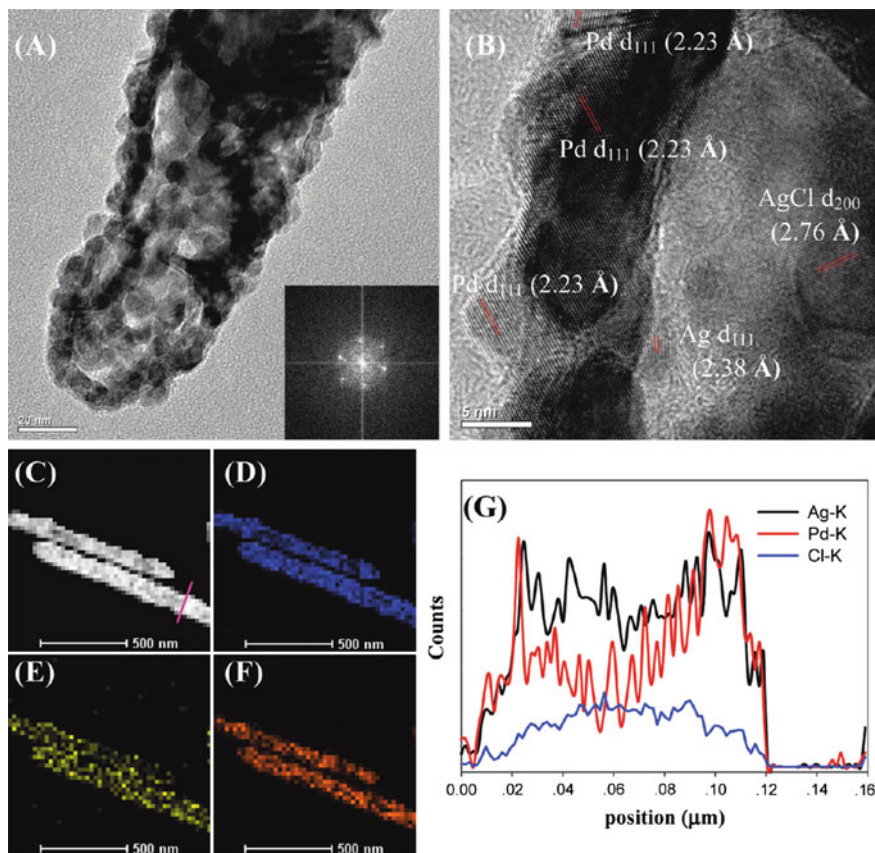
Fig. 18 **a**, **b** HRTEM images of PdAg-25 nanotubes. The *inset* in (**a**) shows the corresponding two-dimensional fast Fourier transform (FFT) pattern. **c** The high-angle annular dark-field (HAADF) STEM image of PdAg-25 nanotubes; the corresponding elemental mapping of Ag (**d**), Pd (**e**), and Cl (**f**) in the PdAg-25 nanotubes. **g** Cross-sectional compositional line profiles of a PdAg-25 nanotube. Reprinted from Ref. [76] with permission by the American Chemical Society

excellent catalytic activity and stability for formic acid oxidation due to their unique 1D nanostructures. In the electrochemical impedance spectroscopy studies, it was also found that the charge-transfer resistance (R_{CT}) at the PdAg-100 nanotubes is much smaller than that at the PdAg-25 nanotubes, indicating the electron-transfer kinetics for formic acid oxidation at the PdAg-100 nanotubes is much better facilitated.

In another study, we synthesized bimetallic PdAg ANWs based on a facile one-step wet chemical strategy [70]. Uniform PdAg nanowires were produced by heating the silver nitrate and $Pd(NO_3)_2 \cdot 2H_2O$ solution in ethylene glycol at 170 °C with the presence of poly(vinyl pyrrolidone). The HRTEM images in Fig. 20a, b
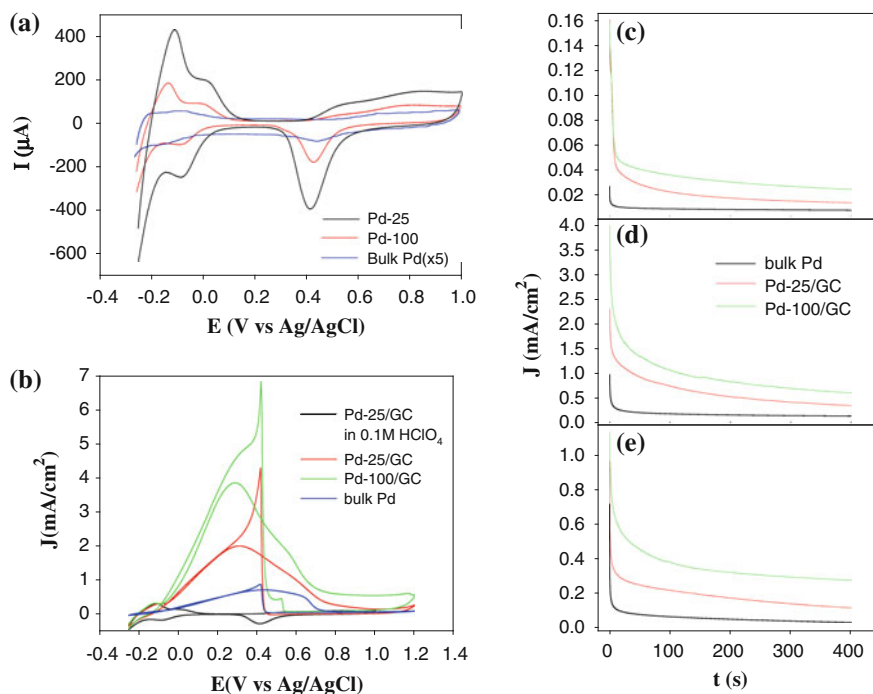
Fig. 19 a Cyclic voltammograms of the PdAg-25/GC (*black curve*), PdAg-100/GC (*red curve*), and bulk Pd electrode (*blue curve*) in 0.1 M HClO$_4$ solution. For comparison, the CV from the Pd bulk electrode is magnified 5×. **b** CVs of the PdAg-25/GC (*red curve*), PdAg-100/GC (*green curve*), and bulk Pd electrode (*blue curve*) electrodes in 0.1 M HClO$_4$ and 0.5 M HCOOH solution and the CV of PdAg-25/GC (*black curve*) in 0.1 M HClO$_4$. Potential scan rate 0.1 V s^{-1}. Chronoamperometric curves of the bulk Pd, PdAg-25/GC and PdAg-100/GC electrodes in 0.1 M HClO$_4$ + 0.5 M HCOOH at different electrode potentials: **c** −0.15, **d** +0.3, and **e** +0.68 V. Reprinted from Ref. [76] with permission by the American Chemical Society

show that worm-like nanowires were formed and the surface of the nanowires is predominated by Pd(111) planes. As mentioned previously, the (111) planes of Pd are less susceptible to oxidation and have a lower peak potential for formic acid oxidation, making the nanowires promising electrocatalysts for DFAFCs. The element maps revealed that the elements of Pd and Ag are homogeneously dispersed in the PdAg nanowires, indicating the formation of alloy structure. The electrochemical studies showed that although the onset potential of formic acid oxidation on PdAg nanowires is only a little more negative than that on the commercial Pd/C catalyst, the current density of formic acid oxidation in both forward and reverse potential sweeps is much larger (about 3.4 times) than that obtained at the Pd/C. Moreover, from the CV and chronoamperometric measurements, our synthesized PdAg nanowires exhibit high CO tolerance and
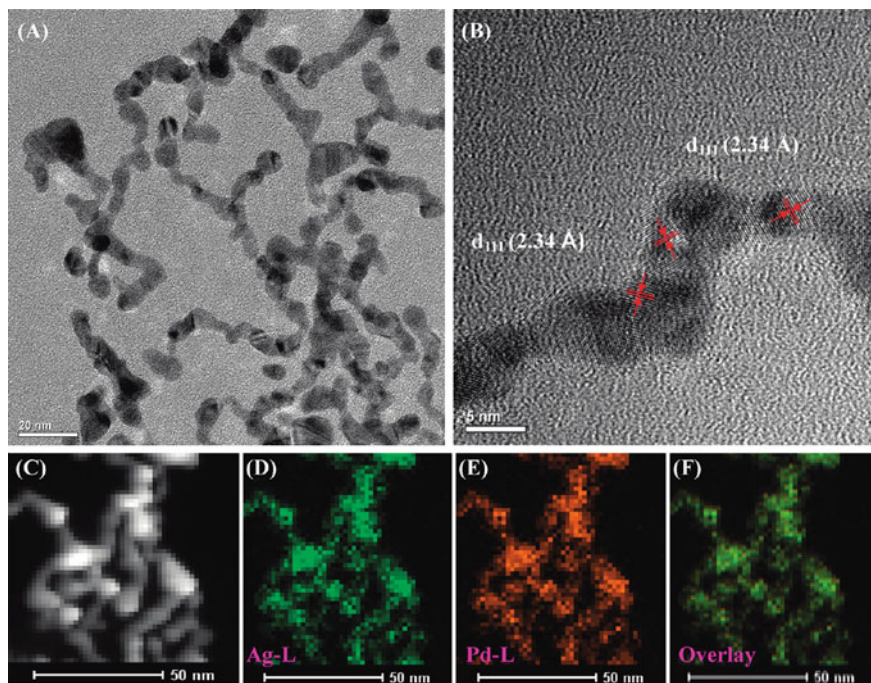
Fig. 20 **a–b** High-resolution TEM micrographs (HRTEM) of PdAg nanowires at different magnifications. The *scale bars* are **a** 20 nm and **b** 5 nm. **c** The high angle annular dark field (HAADF) STEM image of PdAg nanowires and the corresponding elemental mapping of Ag (**d**), Pd (**e**). **f** Overlay map of the elements in the PdAg nanowires. Reprinted from Ref. [70] with permission by the American Chemical Society

long-term electrochemical stability. On the other hand, the electrochemical impedance spectroscopy measurements showed that with the electrode potential increasing the impedance spectra of PdAg nanowires show arcs in the first quadrant firstly and then negative impedance was observed in the second quadrant (Fig. 21a). However, all the impedance spectra of Pd/C are located in the first quadrant within the entire potential range (Fig. 21b). The different impedance results obtained from the two catalysts suggest that PdAg nanowires have higher CO tolerance and fast formic acid oxidation kinetics. Also from Fig. 21c, it can be seen that the R_{CT} derived from PdAg ANWs is remarkably smaller than that from the Pd/C catalysts within the studied potential window. The smaller R_{CT} indicates that the electron-transfer kinetics for formic acid oxidation at the PdAg nanowires is much better facilitated than that at the Pd/C catalysts. All the results demonstrate that the as-synthesized PdAg nanowires have much better catalytic performance than that of commercial Pd/C catalysts.

Fig. 21 Nyquist impedance
plots of formic acid oxidation
on PdAg-NW/GC (**a**) and
Pd/GC (**b**) electrodes in
0.1 M HClO$_4$ +0.5 M
HCOOH at various electrode
potentials. The *solid lines*
show some representative fits
to the experimental data
based on the equivalent
circuits. **c** Charge-transfer
resistance (R_{CT}) of formic
acid electrooxidation at
different electrode potentials
on PdAg-NW/GC (*black
curve*) and Pd/GC (*red curve*)
electrodes. Reprinted from
Ref. [70] with permission by
the American Chemical
Society
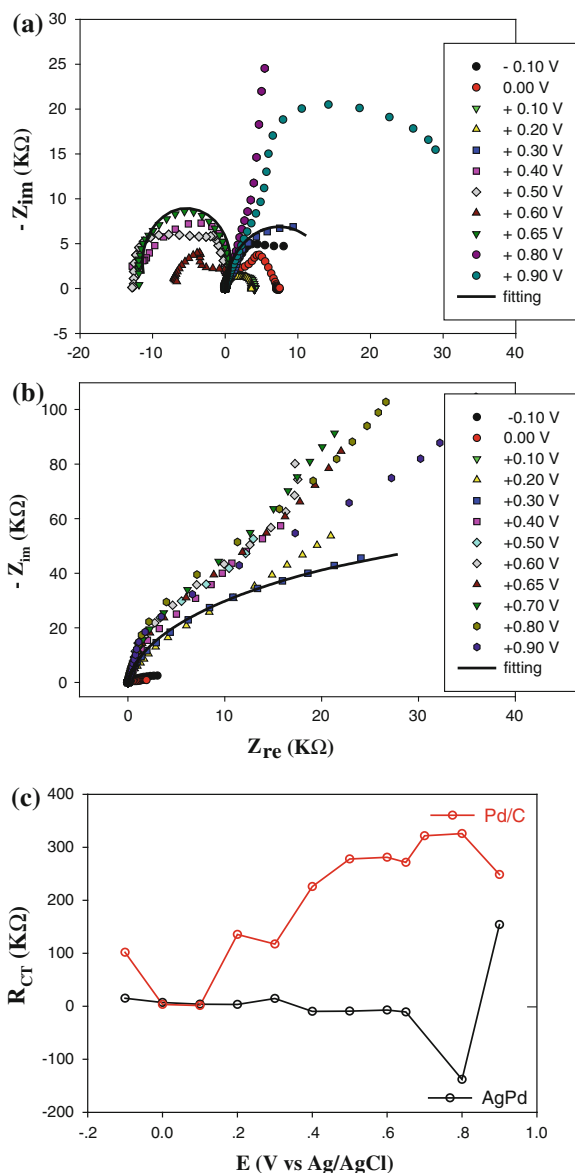
Recently, Song et al. [78] reported the fabrication of Pd nanotube electrodes by
means of electrodeposition method as a function of applied current density. From
the TEM and SEM images (Fig. 22) of the Pd array electrodes electrodeposited
using different current densities, it can be seen that all the products exhibit tubular
arrays having an average diameter of ∼220 nm and different lengths. Note that the
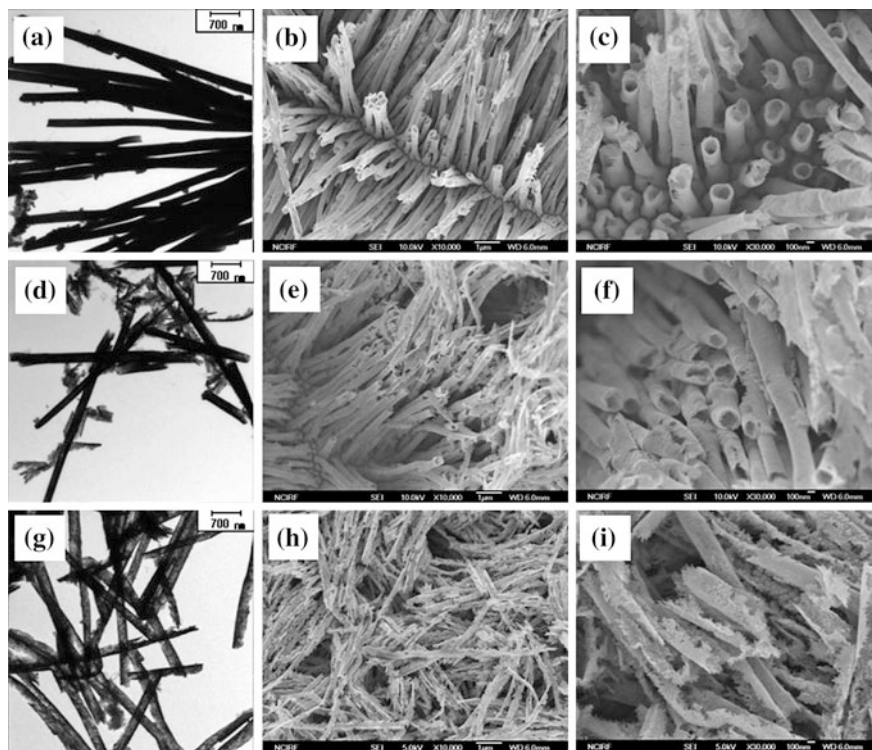surface of the as-synthesized Pd-NT becomes rougher with the increase in current

Fig. 22 TEM and SEM images of the Pd nanotube arrays fabricated at different current densities for 12 h: -1 mA cm^{-2} (Pd-NT-1) (**a**, **b**, **c**); -3 mA cm^{-2} (Pd-NT-3) (**d**, **e**, **f**) and -5 mA cm^{-2} (Pd-NT-5) (**g**, **h**, **i**). Reprinted from Ref. [78] with permission by Elsevier

densities and the Pd-NT-5 tube arrays electrodeposited under the highest applied current density display the roughest surface. This suggests that the fast tube array growth under higher current density may result in rougher surface structure. In the electrocatalytic studies for formic acid oxidation, it was found that the Pd-NT-5 exhibited the largest electrochemical active surface area and the highest electro-catalytic activity among the three samples, but the catalytic activities of all the Pd nanotubes are lower than that of the commercial Pd catalyst (20 wt%). The authors compared the electrochemical stability of the Pd-NT-5 and commercial Pd/C catalyst. As shown in Fig. 23a, the Pd-NT-5 exhibits nearly maintained electro-catalytic activity after the stability test. Simultaneously, the size and morphology of the Pd-NT-5 also remained after the stability test. In contrast, the electrocata-lytic activity of the Pd/C deteriorated significantly after the stability test (Fig. 23b). Furthermore, the Pd/C showed increased particle size and nonuniform size distribution. The results strongly suggest that the Pd nanotubes have enhanced electrocatalytic stability, which may be ascribed to the less aggregation of 1D Pd nanotubes during the catalytic reaction in comparison with the Pd/C.
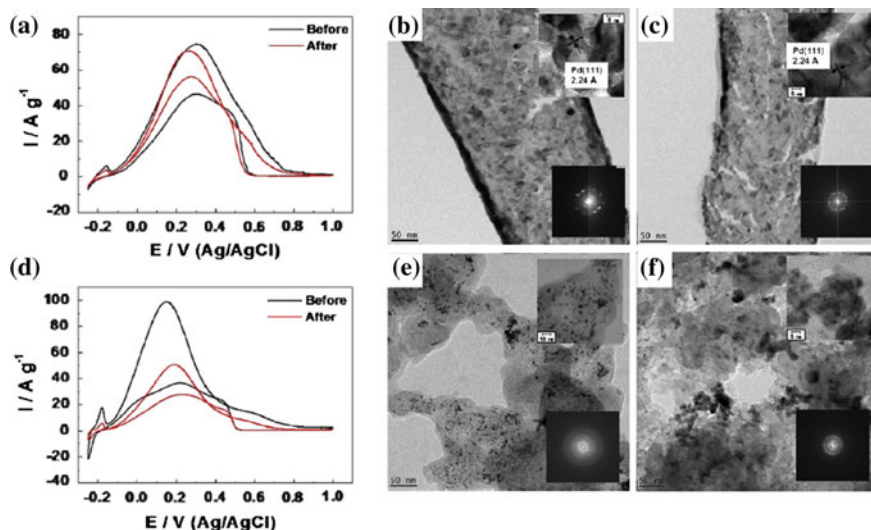
Fig. 23 **a** CVs of Pd-NT-5 before and after stability test in 0.5 M HCOOH and 0.1 M HClO$_4$ at 25 °C. TEM images and transmission electron diffraction (TED) patterns of Pd-NT-5, **b** before and **c** after stability test. **d** CVs of Pd/C before and after stability test in 0.5 M HCOOH and 0.1 M HClO$_4$ at 25 °C. TEM images and TED patterns of Pd/C, **e** before and **f** after stability test. Reprinted from Ref. [78] with permission by Elsevier

4 One-Dimensional Pd-Based Nanomaterials as Effective Hydrogen Storage Materials

Except for the physical methods, such as storage in tanks as compressed hydrogen and physical adsorption on large surface area adsorbents [112–114], chemical materials including metal-borohydrides [115], Mg-based alloys [116], carbon materials [117], and ammonia-boranes [118] etc. have also been widely used as potential hydrogen storage media. However, due to the strong binding between hydrogen and most of the materials, poor dehydrogenation kinetics and high temperatures needed for hydrogen release limit greatly the practical application of these materials. Recently, palladium-based alloys have been found to exhibit higher solubility and permeability of hydrogen than in pure Pd [119–121]. Especially, the nanostructured materials exhibit improved capacity of hydrogen storage compared to the bulk counterparts due to the large surface area and short hydrogen diffusion paths. Similar to the catalytic activity, the hydrogen storage capacity of the Pd-based nanomaterials is strongly related to their structure factors, such as size, composition, and morphology. For example, the previous study showed that for PdAg alloys, the highest permeability for hydrogen was obtained from the alloy with ∼23 wt% of Ag when measured at a pressure of 1 atm and temperature above 473 K [122, 123]. Further simulation study suggested that faster hydrogen
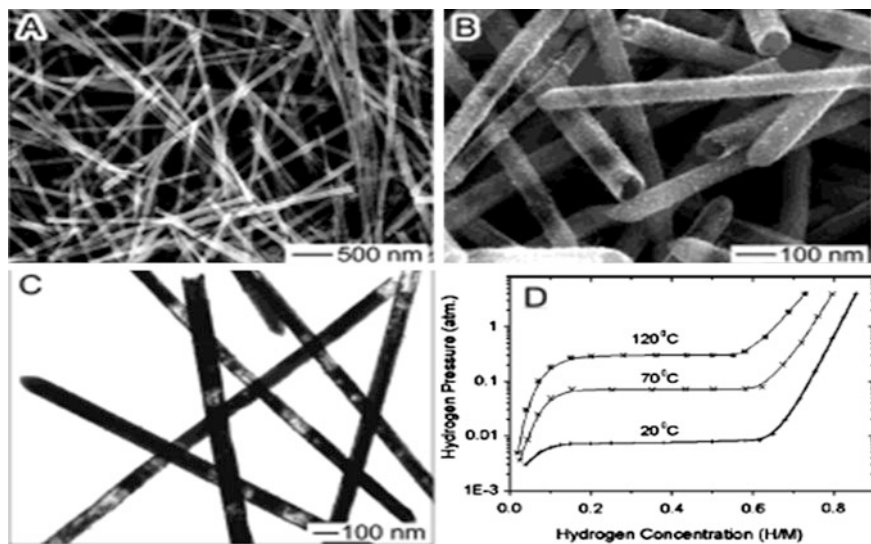
Fig. 24 **a**, **b** SEM images and **c** TEM image of silver nanowires with surface coated with Pd/Ag alloy sheaths. **d** PC isotherms for hydrogen desorption from the hydrides of the as-synthesized Ag@PdAg nanocables at 20, 70, and 120 °C. Here H/M is the hydrogen-to-metal ratio. Reprinted from Ref. [119] with permission by the American Chemical Society

diffusion can be realized from the PdAg alloys with Ag concentration higher than 63 % [124].

Sun et al. [119] synthesized silver nanowires with surface coated by thin sheaths of Pd/Ag alloys through the galvanic replacement reaction. From the SEM and TEM images shown in Fig. 24a–c, each Ag nanowire of ∼60 nm in diameter is coated with Pd/Ag sheaths and is straight and uniform in diameter along the entire long axis. It was found that different from the Pd nanotubes formed from short Ag nanowires, only some segments of the long Ag wire have been converted to hollow structure after galvanic replacement reaction. The total percentage of Ag in the final product was determined to be as high as 92.2 wt%. Figure 24d shows the pressure-composition (PC) isotherms of the as-synthesized Ag/Pd nanostructure (Ag@PdAg) at different temperatures (20, 70, and 120 °C). It can be seen that the distinct plateaus were formed similar to those of polycrystalline Pd powders, indicating the existence of a broad metal-H miscibility gap for the Ag@PdAg wires. Moreover, the absorption and desorption of hydrogen were reversible and the reactions at room temperature were very fast for the Ag@PdAg system. By comparison, the hydrogen solubility of Ag@PdAg wires is larger than that of Pd powers, which can be ascribed to the unique structure of PdAg alloy sheath formed on the Ag nanowires.

Recently, Chen and coworkers [94] reported that the Pd–Cd nanomaterials with 10–15 % Cd exhibit the highest hydrogen storage ability, over 15 times greater than the pure Pd nanoporous materials. In their study, the hydrogen storage ability

Fig. 25 Cyclic voltammograms of the Pd–Cd electrodes in 0.1 M HClO$_4$ performed with a scan rate of 20 mV s^{-1}. The overall hydrogen desorption charge Q_H versus the normalized atomic composition of Cd is shown in the inset. Reprinted from Ref. [94] with permission by the American Chemical Society
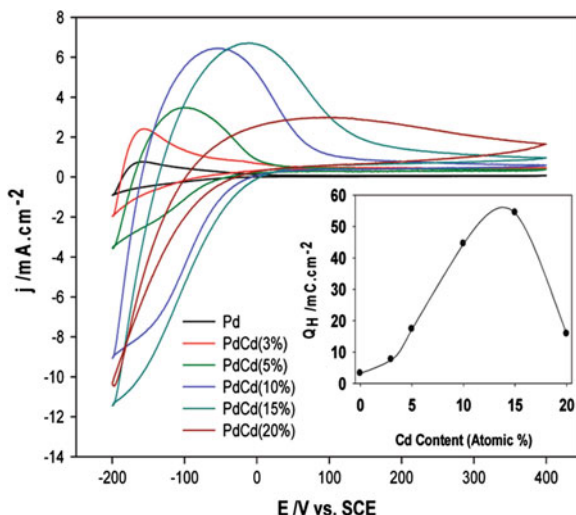
of Pd–Cd nanomaterials with different compositions was evaluated by using electrochemical cyclic voltammetry technique. Under the acid condition, it is easy to clearly separate the region of hydrogen sorption/desorption from the potential of the palladium oxide formation. However, it is not so easy to decouple adsorption from absorption of hydrogen. Thus, they used the total charge, Q_H, obtained by integrating the area under the anodic peaks in the CVs to determine the hydrogen storage ability. As shown in Fig. 25, the charges for hydrogen desorption on the Pd–Cd nanostructures displays a volcano shape with 10–15 % Cd possessing the highest capacity. The authors found that with the amount of Cd increasing from 0 to 15 %, the crystallite size decreased from 25.81 to 9.16 nm and the surface area was increased from 11.58 to 46.64 m^2 g^{-1}. However, when the amount of Cd was further increased to 20 %, larger PdCd nanopartilces were formed and decreased surface area was obtained, thus resulting in the lower hydrogen storage capacity. Therefore, the hydrogen storage ability of the PdCd nanostructures depends on the surface structure and crystallite size. The enhanced hydrogen storage capacity upon the addition of Cd can be ascribed to the formation of small dendritic structures, dilation of the lattice constant, and decrease of the crystalline size.

By using electrochemical cyclic voltammetry, our group studied the hydrogen storage properties of the PdAg nanotubes obtained by galvanic displacement between Ag nanorods and Pd(NO$_3$)$_2$ at different reaction times [125]. From the SEM images (Fig. 26a–d) of the PdAg-(10), PdAg-(90), PdAg-(150) and PdAg-(180) nanotubes, which were collected at reaction times of 10, 90, 150, and 180 min, respectively, the hollow structure could be seen gradually with the reaction time increasing. Based on the inductive coupling high frequency plasma-mass spectrophotometry (ICP-MS) measurements, the ratios of Pd to Ag with 5:95, 10:90, 15:85, and 18:82 were determined for the samples. That is, the Pd content in the PdAg nanotubes increases with the increase ingalvanic reaction time. In the
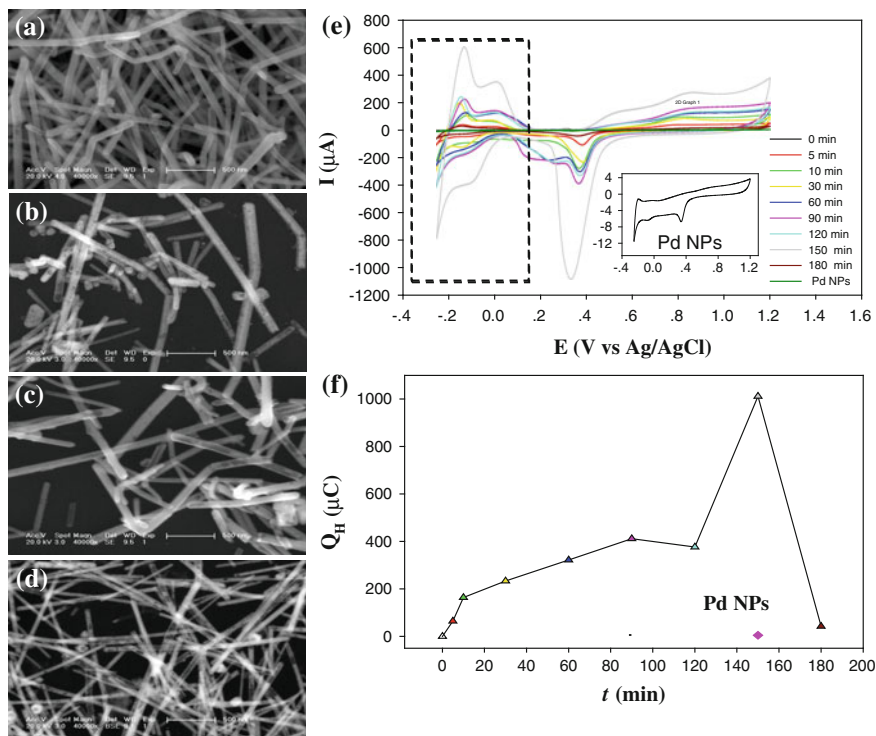
Fig. 26 Scanning electron microscopy (SEM) images of the PdAg nanotubes synthesized with different galvanic reaction times: 10 min (**a**); 90 min (**b**); 150 min (**c**) and 180 min (**d**). **e** Cyclic voltammograms of the PdAg nanotubes obtained at different galvanic reaction times and Pd nanoparticles in 0.1 M HClO$_4$ electrolyte solution. Potential scan rate 0.1 V s^{-1}. For clarity, the CV from Pd nanoparticles is shown in the *inset*. The *dashed frame* shows the hydrogen adsorption-desorption region obtained on the PdAg nanotubes. **f** The total charge (Q_H) of hydrogen adsorption and absorption on the PdAg nanotubes dependent on galvanic reaction time. Reprinted from Ref. [125] with permission by the Royal Society of Chemistry

CVs (Fig. 26e) of the synthesized PdAg nanotubes in a N$_2$ saturated 0.1 M HClO$_4$ aqueous solution, there is obvious hydrogen adsorption/desorption in the potential range of −0.25 to +0.1 V. From the dependence of Q_H on reaction time shown in Fig. 26f, it can be seen clearly that the hydrogen storage ability depends strongly on the composition of the PdAg nanostructured materials. The PdAg nanotubes with 15 % Pd possess the highest capacity for hydrogen absorption, which is over 200 times higher than that of pure Pd nanoparticles. Such significantly enhanced ability for hydrogen storage can be ascribed to the special tubular structures and alloying of Pd and Ag around the walls of the nanostructures. This work suggests that 1D Pd-based alloy nanotubes with low Pd content might represent a unique class of low-cost materials for efficient hydrogen storage.

5 Conclusions and Future Outlook

In this chapter, we discussed the technological challenges of the modern electrocatalysts and summarized recent research progress of 1D Pd-based nanomaterials as efficient electrocatalysts on both anode and cathode sides of fuel cells and the applications in hydrogen storage. Specifically, we presented the effect of structural parameters of Pd-based 1D nanomaterials on their electrocatalytic activities for cathode ORR, and anode small molecules (methanol, ethanol, and formic acid) oxidation, and on their hydrogen storage capacity. From the studies shown in this chapter, it can be concluded that 1D Pd-based nanomaterials exhibit enhanced electrocatalytic activity and improved electrochemical stability for oxygen reduction and small molecule oxidation. Except for the large electrochemically active surface area of 1D nanomaterials, the unique anisotropic structure of nanowire, nanorod, and nanotube can also facilitate the mass and electron-transfer during the catalytic reactions. Meanwhile, it has been found that 1D Pd-based nanomaterials possess excellent hydrogen storage ability compared to the corresponding 0D structures. Therefore, 1D Pd-based nanomaterials represent not only a class of non-Pt electrocatalysts with low cost and excellent catalytic performance, but also a class of novel hydrogen storage materials for fuel cells.

Yet, despite substantial progress in the electrocatalysts based on 1D Pd-based nanomaterials, some challenges remain in future work in this field. The emphases of future investigations should mainly include: (1) further developing different synthetic techniques to produce high quality 1D Pd-based nanomaterials with controlled size, shape, and composition; (2) further improving the catalytic performance and reducing Pd loading of 1D nanomaterials to achieve cost-effective fuel cell electrocatalysts; (3) further investigating theoretically the correlation between structures of 1D Pd-based materials and their catalytic and hydrogen storage properties to provide fundamental direction for nanomaterial design; (4) further enhancing the study of 1D Pd-based nanocatalysts in real fuel cells to test their catalytic performance in practical applications.

References

1. Dresselhaus MS, Thomas IL (2001) Nature 414(6861):332–337
2. Dillon R, Srinivasan S, Arico AS, Antonucci V (2004) J Power Sources 127(1–2):112–126
3. Lamy C, Lima A, LeRhun V, Delime F, Coutanceau C, Leger JM (2002) J Power Sources 105(2):283–296
4. Okada O, Yokoyama K (2001) Fuel Cells 1(1):72–77
5. Winter M, Brodd RJ (2004) Chem Rev 104(10):4245–4269

6. Vielstich W, Lamm A, Gasteiger HA (2003) Handbook of fuel cells: fundamentals, technology, and applications, vol 4. Wiley, Chichester
7. Chen AC, Holt-Hindle P (2010) Chem Rev 110(6):3767–3804
8. Chen W, Kim JM, Sun SH, Chen SW (2007) Langmuir 23(22):11303–11310
9. Zhang J, Yang HZ, Yang KK, Fang J, Zou SZ, Luo ZP, Wang H, Bae IT, Jung DY (2010) Adv Funct Mater 20(21):3727–3733
10. Yang HZ, Zhang J, Sun K, Zou SZ, Fang JY (2010) Angew Chem Int Ed 49(38):6848–6851
11. Chen W, Kim JM, Xu LP, Sun SH, Chen SW (2007) J Phys Chem C 111(36):13452–13459
12. Stamenkovic VR, Fowler B, Mun BS, Wang GF, Ross PN, Lucas CA, Markovic NM (2007) Science 315(5811):493–497
13. Xia BY, Wu HB, Wang X, Lou XW (2012) J Am Chem Soc 134(34):13934–13937
14. Chen W, Chen SW (2011) J Mater Chem 21(25):9169–9178
15. Chen W, Kim JM, Sun SH, Chen SW (2008) J Phys Chem C 112(10):3891–3898
16. Chen W, Kim J, Sun SH, Chen SW (2006) Phys Chem Chem Phys 8(23):2779–2786
17. Kang YJ, Murray CB (2010) J Am Chem Soc 132(22):7568–7569
18. Gasteiger HA, Markovic N, Ross PN, Cairns EJ (1994) J Electrochem Soc 141(7):1795–1803
19. Dinh HN, Ren XM, Garzon FH, Zelenay P, Gottesfeld S (2000) J Electroanal Chem 491(1–2):222–233
20. Oetjen HF, Schmidt VM, Stimming U, Trila F (1996) J Electrochem Soc 143(12):3838–3842
21. Frelink T, Visscher W, vanVeen JAR (1996) Langmuir 12(15):3702–3708
22. Goodenough JB, Hamnett A, Kennedy BJ, Manoharan R, Weeks SA (1988) J Electroanal Chem 240(1–2):133–145
23. Chen W, Xu LP, Chen SW (2009) J Electroanal Chem 631(1–2):36–42
24. Lu YZ, Chen W (2011) Chem Commun 47(9):2541–2543
25. Lim B, Jiang MJ, Camargo PHC, Cho EC, Tao J, Lu XM, Zhu YM, Xia YN (2009) Science 324(5932):1302–1305
26. Chen W, Chen SW (2009) Angew Chem Int Edit 48(24):4386–4389
27. Chen W, Ny D, Chen SW (2010) J Power Sources 195(2):412–418
28. Liu HS, Song CJ, Tang YH, Zhang JL, Zhang HJ (2007) Electrochim Acta 52(13):4532–4538
29. Zhang L, Zhang JJ, Wilkinson DP, Wang HJ (2006) J Power Sources 156(2):171–182
30. Morozan A, Jousselme B, Palacin S (2011) Energy Environ Sci 4(4):1238–1254
31. Chen ZW, Higgins D, Yu AP, Zhang L, Zhang JJ (2011) Energy Environ Sci 4(9):3167–3192
32. Wei WT, Lu YZ, Chen W, Chen SW (2011) J Am Chem Soc 133(7):2060–2063
33. Lu YZ, Wang YC, Chen W (2011) J Power Sources 196(6):3033–3038
34. Wu HB, Chen W (2011) J Am Chem Soc 133(39):15236–15239
35. Serov A, Kwak C (2009) Appl Catal B Environ 91(1–2):1–10
36. Serov A, Kwak C (2009) Appl Catal B Environ 90(3–4):313–320
37. Lu YZ, Chen W (2012) Chem Soc Rev 41(9):3594–3623
38. Antolini E (2009) Energy Environ Sci 2(9):915–931
39. Bianchini C, Shen PK (2009) Chem Rev 109(9):4183–4206
40. Cheng TT, Gyenge EL (2009) J Appl Electrochem 39(10):1925–1938
41. Zhou WP, Lewera A, Larsen R, Masel RI, Bagus PS, Wieckowski A (2006) J Phys Chem B 110(27):13393–13398
42. Larsen R, Ha S, Zakzeski J, Masel RI (2006) J Power Sources 157(1):78–84
43. Mazumder V, Sun SH (2009) J Am Chem Soc 131(13):4588–4589
44. Xiao L, Zhuang L, Liu Y, Lu JT, Abruna HD (2009) J Am Chem Soc 131(2):602–608
45. Chen XM, Lin ZJ, Jia TT, Cai ZM, Huang XL, Jiang YQ, Chen X, Chen GN (2009) Anal Chim Acta 650(1):54–58
46. Fu Y, Wei ZD, Chen SG, Li L, Feng YC, Wang YQ, Ma XL, Liao MJ, Shen PK, Jiang SP (2009) J Power Sources 189(2):982–987

47. Hu FP, Chen CL, Wang ZY, Wei GY, Shen PK (2006) Electrochim Acta 52(3):1087–1091
48. Wei WT, Chen W (2012) J Power Sources 204:85–88
49. Jiang YY, Lu YZ, Li FH, Wu TS, Niu L, Chen W (2012) Electrochem Commun 19:21–24
50. Chen XM, Wu GH, Chen JM, Chen X, Xie ZX, Wang XR (2011) J Am Chem Soc 133(11):3693–3695
51. Zhang J, Fang JY (2009) J Am Chem Soc 131(51):18543–18547
52. Bergamaski K, Pinheiro ALN, Teixeira-Neto E, Nart FC (2006) J Phys Chem B 110(39):19271–19279
53. Mayrhofer KJJ, Blizanac BB, Arenz M, Stamenkovic VR, Ross PN, Markovic NM (2005) J Phys Chem B 109(30):14433–14440
54. Tian N, Zhou ZY, Sun SG, Ding Y, Wang ZL (2007) Science 316(5825):732–735
55. Fernandez JL, Walsh DA, Bard AJ (2005) J Am Chem Soc 127(1):357–365
56. Suo YG, Zhuang L, Lu JT (2007) Angew Chem Int Edit 46(16):2862–2864
57. Schmidt TJ, Jusys Z, Gasteiger HA, Behm RJ, Endruschat U, Boennemann H (2001) J Electroanal Chem 501(1–2):132–140
58. Jiang L, Hsu A, Chu D, Chen R (2010) Electrochim Acta 55(15):4506–4511
59. Shao MH, Sasaki K, Adzic RR (2006) J Am Chem Soc 128(11):3526–3527
60. Jung CH, Sanchez-Sanchez CM, Lin CL, Rodriguez-Lopez J, Bard AJ (2009) Anal Chem 81(16):7003–7008
61. Fernandez JL, Raghuveer V, Manthiram A, Bard AJ (2005) J Am Chem Soc 127(38):13100–13101
62. Maiyalagan T, Scott K (2010) J Power Sources 195(16):5246–5251
63. He QG, Chen W, Mukerjee S, Chen SW, Laufek F (2009) J Power Sources 187(2):298–304
64. Zhu CZ, Guo SJ, Dong SJ (2012) Adv Mater 24(17):2326–2331
65. Zhu CZ, Guo SJ, Dong SJ (2012) J Mater Chem 22(30):14851–14855
66. Koenigsmann C, Sutter E, Chiesa TA, Adzic RR, Wong SS (2012) Nano Lett 12(4):2013–2020
67. Guo SJ, Dong SJ, Wang EK (2010) Chem Commun 46(11):1869–1871
68. Ksar F, Surendran G, Ramos L, Keita B, Nadjo L, Prouzet E, Beaunier P, Hagege A, Audonnet F, Remita H (2009) Chem Mater 21(8):1612–1617
69. Xu CW, Wang H, Shen PK, Jiang SP (2007) Adv Mater 19(23):4256–4259
70. Lu YZ, Chen W (2012) ACS Catal 2(1):84–90
71. Cheng FL, Wang H, Sun ZH, Ning MX, Cai ZQ, Zhang M (2008) Electrochem Commun 10(5):798–801
72. Wang H, Xu CW, Cheng FL, Zhang M, Wang SY, Jiang SP (2008) Electrochem Commun 10(10):1575–1578
73. Li WZ, Haldar P (2009) Electrochem Commun 11(6):1195–1198
74. Zhang ZY, More KL, Sun K, Wu ZL, Li WZ (2011) Chem Mater 23(6):1570–1577
75. Chen ZW, Waje M, Li WZ, Yan YS (2007) Angew Chem Int Edit 46(22):4060–4063
76. Lu YZ, Chen W (2010) J Phys Chem C 114(49):21190–21200
77. Xu CX, Zhang Y, Wang LQ, Xu LQ, Bian XF, Ma HY, Ding Y (2009) Chem Mater 21(14):3110–3116
78. Song YJ, Lee YW, Han SB, Park KW (2012) Mater Chem Phys 134(2–3):567–570
79. Alia SM, Jensen KO, Pivovar BS, Yan YS (2012) ACS Catal 2(5):858–863
80. Cui CH, Yu JW, Li HH, Gao MR, Liang HW, Yu SH (2011) ACS Nano 5(5):4211–4218
81. Koenigsmann C, Wong SS (2011) Energy Environ Sci 4(4):1161–1176
82. Huang XQ, Zheng NF (2009) J Am Chem Soc 131(13):4602–4603
83. Hoshi N, Kida K, Nakamura M, Nakada M, Osada K (2006) J Phys Chem B 110(25):12480–12484
84. Baldauf M, Kolb DM (1996) J Phys Chem 100(27):11375–11381
85. Smith PA, Nordquist CD, Jackson TN, Mayer TS, Martin BR, Mbindyo J, Mallouk TE (2000) Appl Phys Lett 77(9):1399–1401
86. Xia YN, Yang PD, Sun YG, Wu YY, Mayers B, Gates B, Yin YD, Kim F, Yan YQ (2003) Adv Mater 15(5):353–389

87. Garbarino S, Ponrouch A, Pronovost S, Gaudet J, Guay D (2009) Electrochem Commun 11(10):1924–1927
88. Reece SY, Hamel JA, Sung K, Jarvi TD, Esswein AJ, Pijpers JJH, Nocera DG (2011) Science 334(6056):645–648
89. Kudo A, Miseki Y (2009) Chem Soc Rev 38(1):253–278
90. Youngblood WJ, Lee SHA, Maeda K, Mallouk TE (2009) Acc Chem Res 42(12):1966–1973
91. Li Y, Zhang JZ (2010) Laser Photonics Rev 4(4):517–528
92. Maeda K, Domen K (2010) J Phys Chem Lett 1(18):2655–2661
93. Kruk M, Jaroniec M (2001) Chem Mater 13(10):3169–3183
94. Adams BD, Wu GS, Nigrio S, Chen AC (2009) J Am Chem Soc 131(20):6930–6931
95. Yeager E (1984) Electrochim Acta 29(11):1527–1537
96. Stamenkovic V, Mun BS, Mayrhofer KJJ, Ross PN, Markovic NM, Rossmeisl J, Greeley J, Norskov JK (2006) Angew Chem Int Edit 45(18):2897–2901
97. Koenigsmann C, Santulli AC, Gong KP, Vukmirovic MB, Zhou WP, Sutter E, Wong SS, Adzic RR (2011) J Am Chem Soc 133(25):9783–9795
98. Sarkar A, Murugan AV, Manthiram A (2008) J Phys Chem C 112(31):12037–12043
99. Liu HS, Song CJ, Zhang L, Zhang JJ, Wang HJ, Wilkinson DP (2006) J Power Sources 155(2):95–110
100. Jin MS, Liu HY, Zhang H, Xie ZX, Liu JY, Xia YN (2011) Nano Res 4(1):83–91
101. Lee YW, Ko AR, Han SB, Kim HS, Kim DY, Kim SJ, Park KW (2010) Chem Commun 46(48):9241–9243
102. Wu HX, Li HJ, Zhai YJ, Xu XL, Jin YD (2012) Adv Mater 24(12):1594–1597
103. Sun SH, Zhang GX, Geng DS, Chen YG, Li RY, Cai M, Sun XL (2011) Angew Chem Int Edit 50(2):422–426
104. Guo SJ, Zhang S, Sun XL, Sun SH (2011) J Am Chem Soc 133(39):15354–15357
105. Xu CW, Cheng LQ, Shen PK, Liu YL (2007) Electrochem Commun 9(5):997–1001
106. Roudgar A, Gross A (2004) Surf Sci 559(2–3):L180–L186
107. Capon A, Parsons R (1973) J Electroanal Chem 45(2):205–231
108. Neurock M, Janik M, Wieckowski A (2008) Faraday Discuss 140:363–378
109. Samjeske G, Miki A, Ye S, Osawa M (2006) J Phys Chem B 110(33):16559–16566
110. Kang YJ, Qi L, Li M, Diaz RE, Su D, Adzic RR, Stach E, Li J, Murray CB (2012) ACS Nano 6(3):2818–2825
111. Miyake H, Okada T, Samjeske G, Osawa M (2008) Phys Chem Chem Phys 10(25):3662–3669
112. McKeown NB, Budd PM (2006) Chem Soc Rev 35(8):675–683
113. Rosi NL, Eckert J, Eddaoudi M, Vodak DT, Kim J, O'Keeffe M, Yaghi OM (2003) Science 300(5622):1127–1129
114. Zhao XB, Xiao B, Fletcher AJ, Thomas KM, Bradshaw D, Rosseinsky MJ (2004) Science 306(5698):1012–1015
115. Nakamori Y, Li HW, Matsuo M, Miwa K, Towata S, Orimo S (2008) J Phys Chem Solids 69(9):2292–2296
116. Bardhan R, Ruminski AM, Brand A, Urban JJ (2011) Energy Environ Sci 4(12):4882–4895
117. Pumera M (2011) Energy Environ Sci 4(3):668–674
118. Stephens FH, Baker RT, Matus MH, Grant DJ, Dixon DA (2007) Angew Chem Int Edit 46(5):746–749
119. Sun YG, Tao ZL, Chen J, Herricks T, Xia YN (2004) J Am Chem Soc 126(19):5940–5941
120. Kobayashi H, Yamauchi M, Kitagawa H, Kubota Y, Kato K, Takata M (2008) J Am Chem Soc 130(6):1818–1819
121. Kobayashi H, Yamauchi M, Kitagawa H, Kubota Y, Kato K, Takata M (2010) J Am Chem Soc 132(16):5576–5577
122. Weiss A, Ramaprabhu S, Rajalakshmi N (1997) Z Phys Chem 199:165–212
123. Uemiya S, Matsuda T, Kikuchi E (1991) J Membr Sci 56(3):315–325
124. Barlag H, Opara L, Zuchner H (2002) J Alloys Compd 330:434–437
125. Lu YZ, Jin RT, Chen W (2011) Nanoscale 3(6):2476–2480